

1
2 **Volcanic Emissions, Plume Dispersion and Downwind Radiative Impacts following**
3 **Mount Etna Series of Eruptions of 21-26 February 2021**

4 **P. Sellitto¹, G. Salerno², S. Corradini³, I. Xueref-Remy⁴, A. Riandet⁴, C. Bellon⁴, S.**
5 **Khaykin⁵, G. Ancellet⁵, S. Lolli⁶, E. J. Welton⁷, A. Boselli⁶, A. Sannino⁸, J. Cuesta¹, H.**
6 **Guermazi¹, M. Eremenko¹, L. Merucci³, D. Stelitano³, L. Guerrieri³, and B. Legras⁹**

7 ¹ Univ. Paris Est Créteil and Université de Paris, CNRS, Laboratoire Interuniversitaire des
8 Systèmes Atmosphériques, Institut Pierre Simon Laplace, Créteil, France

9 ²Istituto Nazionale di Geofisica e Vulcanologia, Osservatorio Etno, Catania, Italy.

10 ³Istituto Nazionale di Geofisica e Vulcanologia, Osservatorio Nazionale Terremoti, Rome, Italy

11 ⁴Aix Marseille Univ, Avignon Université, CNRS, IRD, Institut Méditerranéen de Biodiversité et
12 d'Écologie marine et continentale (IMBE), Marseille, France

13 ⁵Laboratoire Atmosphères, Milieux, Observations Spatiales, UMR CNRS 8190, IPSL, Sorbonne
14 Univ./UVSQ, Guyancourt, France

15 ⁶Consiglio Nazionale delle Ricerche – Istituto di Metodologie per l'Analisi Ambientale (CNR-
16 IMAA), C. da S. Loja, Tito Scalo, Potenza, Italy

17 ⁷NASA Goddard Space Flight Center, Code 612, Greenbelt, MD 20771, USA

18 ⁸Dipartimento di Fisica “Ettore Pancini”, Università Federico II di Napoli, Complesso
19 Universitario di Monte S. Angelo, Via Cintia, I-80126 Napoli (Italy).

20 ⁹Laboratoire de Météorologie Dynamique, UMR CNRS 8539, École Normale Supérieure, PSL
21 Research University, École Polytechnique, Sorbonne Universités, École des Ponts PARISTECH,
22 Institut Pierre Simon Laplace, Paris, France

23 Corresponding author: first and last name (pasquale.sellitto@lisa.ipsl.fr)

24 **Key Points:**

- 25 ● Three distinct paroxysmal events took place at Mount Etna from 21 to 26 February 2021
26 and the plumes were transported towards the north
- 27 ● Plumes dispersion is characterized with Lagrangian modelling initialized with measured
28 SO₂ emissions and with satellite observations
- 29 ● A series of LiDARs detected and characterized the plumes downwind and their
30 observations are used to estimate the plumes radiative forcing
- 31

32 **Abstract**

33 During the extended activity of Mount Etna volcano in February-April 2021, three distinct
34 paroxysmal events took place from 21 to 26 February, which were associated with a very
35 uncommon transport of the injected upper-tropospheric plumes towards the north. Using a synergy
36 of observations and modelling, we characterised the emissions and three-dimensional dispersion
37 for these three plumes, we monitor their downwind morphological and optical properties, and we
38 estimate their radiative impacts at selected locations. With a satellite-based source inversion, we
39 estimate the emitted sulphur dioxide (SO₂) mass at an integrated value of 55 kt and plumes
40 injections at up to 12 km altitudes, which combine to qualify this series as extreme in the eruption
41 strengths spectrum for Mount Etna. We then combine Lagrangian dispersion modelling, initialised
42 with measured temporally-resolved SO₂ emission fluxes and altitudes, with satellite observations
43 to track the dispersion of the three individual plumes. The transport towards the north allowed the
44 height-resolved downwind monitoring of the plumes at selected observatories in France, Italy and
45 Israel, using LiDARs and photometric aerosol observations. Volcanic-specific aerosol optical
46 depths in the visible spectral range ranging from about 0.004 to 0.03 and local daily average
47 shortwave radiative forcing ranging from about -0.2 to -1.2 W/m² (at the top of atmosphere) and
48 from about -0.2 to -3.5 W/m² (at the surface) are found. Both the aerosol optical depth and the
49 radiative forcing of the plume depends strongly on its morphology (position of the sampled section
50 of the plume) and composition (possible presence of fine ash).

51 **Plain Language Summary**

52 The volcanic plumes from Mount Etna's eruptions disperse usually towards the east, to the
53 Central-Eastern Mediterranean, where no ground stations are available to monitor and
54 characterise them. During the extended intense volcanic activity of Mount Etna in February-
55 April 2021, some of the plumes dispersed towards the north, in an area where many and well-
56 equipped ground observatories are available. This was a unique and very uncommon possibility
57 to study the emissions, dispersion dynamics, shape/composition and impacts of Mount Etna's
58 emissions. We analysed these rare events using all available information layers: satellite
59 observations, numerical simulation of the plume's dispersion and downwind ground-based
60 observatories. By coupling these information pieces, we could reconstruct these events and
61 untangle their impacts from those of a major Saharan dust outbreak that occurred simultaneously.
62 These events were found quite extreme for the Mediterranean volcanism (extreme emissions and
63 at altitudes as high as 12 km). We found that this kind of volcanic eruptions have a relevant (and
64 not yet studied) impact on the upper-tropospheric composition and regional climate in the
65 Mediterranean area. The plumes, after regional-to-continental dispersion, exhibit a complex
66 filamentary morphology and, and most likely, a complex composition coming from the interplay
67 of sulphur compounds and ash emissions.

68 **1 Introduction**

69 Volcanic activity, spanning from passive degassing to explosive eruptions, can have relevant
70 downwind impacts on the atmospheric composition (e.g. von Glasow et al., 2009), aerosol
71 properties (e.g. Sellitto et al., 2017), air quality and health (e.g. Michaud et al., 2005), the formation
72 and lifetime of clouds (e.g. Malavelle et al., 2017) and the radiative balance (e.g. Andersson et al.,
73 2015, Sellitto et al., 2020, Kloss et al., 2021). Associated with the volcanic activity are both
74 primary emissions of gases and particles, like water vapour, carbon dioxide, sulphur dioxide (SO₂)
75 and ash, and secondary aerosols, in particular the tiny-sized sulphate aerosols (SA) forming from

76 the gaseous- and liquid-phase oxidation/nucleation from SO₂ primary emissions. All these
77 effluents can have environmental and climatic impacts downwind the dispersion pathways of the
78 volcanic plumes. The SA, in particular, are the main contributors of the volcanogenic modulation
79 of the Earth's radiative balance and, then, of the local, regional or global climate system (Sellitto
80 and Briole, 2015). This is due to their high reflectivity properties in the solar spectral range,
81 mirrored by their very high single scattering albedo (SSA) (Krotkov et al., 1997), and their
82 relatively long atmospheric residence time, linked to their tiny typical sizes (Stevenson et al.,
83 2003). While the importance of moderate-to-strong volcanic eruptions, with plume injection in the
84 stratosphere, on the Earth's climate system is now relatively well established (Santer et al., 2014;
85 Ridley et al., 2017), the role on the regional climate system of smaller eruptions, with injection in
86 the troposphere, as well as local impacts of persistent passive degassing activity (Sellitto et al.,
87 2020), is not yet well understood and quantified (Oppenheimer et al., 2011).

88 The downwind impacts of tropospheric volcanic plumes and their spatio-temporal extent depend
89 critically on the interplay of three main aspects: 1) the internal geochemical and geophysical
90 processes linked to magma degassing and plume injection, and, once the plume is released, 2) its
91 atmospheric physico-chemical evolution, and 3) the local and regional atmospheric dynamics
92 driving the plume dispersion. To characterise these three components of the plumes release and
93 evolution, as well as to estimate downwind impacts, a coordinated synergy of ground-based and
94 satellite observations, and the modelling of transport and physical-chemical evolution, are
95 necessary. Such synergies have been exploited in a number of studies in the past (e.g. Haywood et
96 al., 2010; Webley et al., 2012; Sellitto et al., 2016; Kloss et al., 2021).

97 In this paper, we couple ground-based and satellite observations with dispersion and impact
98 modelling to study a specific phase of the extended activity of Mount Etna occurring during the
99 period February-April 2021. We focus, in particular, on the series of paroxysmal eruptions during
100 the period from 21 to 26/02/2021. This period was characterized by an uncommon local dynamics
101 that allowed a rare transport of the emitted plumes towards the north, where a number of ground-
102 based observatories could be used to monitor the morphological, optical and radiative properties
103 of the plumes. Vertically-resolved information can be retrieved from stations equipped with
104 LiDAR (Light Detection And Ranging) systems. From several points of view, this is a unique case-
105 study to gather better insights into the evolution of a moderate volcanic eruption: the extended
106 period of the activity, the unusual intensity of the eruptions, the relatively high altitude of the
107 atmospheric injection and the transport towards areas with a relatively large density of potential
108 downwind observations. Here we show that, in such conditions, a synergistic
109 observational/modelling approach can contribute a more complete end-to-end characterisation of
110 the volcanic events, from emissions to dispersion to downwind impacts.

111 The paper is organized as follows. In Sect. 2 we introduce and describe the array of observations
112 and modelling tools used in this work. In Sect. 3 we provide a qualitative description of the eruptive
113 series under investigation, and we frame this volcanic activity into the wider Mount Etna's internal
114 geophysical context. In Sect. 4 we show results for the characterisation of the emission, dispersion
115 and impacts of this series of events. We draw conclusions in Sect. 5.

116 **2 Data and Methods**

117 2.1 Volcanic SO₂ emission flux rates and total mass estimations from satellite-based source 118 inversion

119 The SO₂ emission flux rates time series and total mass have been obtained by exploiting the
120 measurements collected from the Spinning Enhanced Visible and InfraRed Imager (SEVIRI). The
121 SEVIRI instrument is a multispectral imager on board the Meteosat Second Generation (MSG)
122 geostationary satellite. It has 12 spectral channels from visible to Thermal InfraRed (TIR) spectral
123 ranges and a spatial resolution of 3 km at sub-satellite point. The temporal resolution varies from
124 5 (rapid scan mode over Europe and Northern Africa) to 15 min (Earth full disk) (see
125 <https://www.eumetsat.int/meteosat-second-generation> for more details on MSG platform and
126 SEVIRI instrument). The SEVIRI measurements are collected in real time from the Multimission
127 Acquisition SysTem (MAST) developed at Istituto Nazionale di Geofisica e Vulcanologia (INGV)
128 (Stelitano et al., 2020). All the SEVIRI images used in this work have been resampled in a regular
129 grid of 3×3 km² and processed every 15 minutes.

130 The SO₂ columnar abundance is computed by applying the Volcanic Plume Retrieval (VPR)
131 procedure (Guerrieri et al., 2015). This approach is based on the computations of the plume
132 transmittances in the SEVIRI TIR bands centred at 8.7, 10.8, and 12 μm, obtained through linear
133 equations based on the original image radiances and a new image with volcanic plume signal
134 removed; the latter is computed by means of a linear regression of the radiance values outside the
135 edges of the plume itself. The SO₂ estimates are obtained from 8.7 μm transmittances, after
136 eliminating the contribution of ash and ice particles computed from 10.8 and 12 μm channels. The
137 main advantage of VPR is that the only input required is the volcanic cloud top height.

138 From the SO₂ abundance, the SO₂ emission flux rate is obtained by applying the “traverse
139 approach” (Corradini et al., 2008; Merucci et al., 2011) considering a transect placed at 30±1.5 km
140 from the summit craters and a wind speed derived from the ARPA (Agenzia Regionale per la
141 Protezione Ambientale) database (Scollo et al., 2009). Such a distance for the reference transect
142 has been selected to minimize the retrieval uncertainties induced by both the opacity of the pixels
143 too close to the craters and the dilution of the pixels too far from the emission. Knowing the wind
144 speed, the SO₂ flux at 30 km is then reported to 0 km over the vents (Corradini et al., 2020; 2021).
145 From SO₂ emission rate, the SO₂ total emitted mass is obtained by temporal integration.

146 The volcanic cloud top height is obtained by applying the consolidated “dark pixel” procedure
147 (Prata et al., 2001; Scollo et al., 2014; Corradini et al., 2018) , based on the comparison between
148 the minimum SEVIRI 10.8 μm brightness temperature of a pixel contained in a fixed area over the
149 summit craters and an atmospheric temperature profile measured approximately in the same area
150 and at the same time of satellite acquisition (Scollo et al., 2014; Corradini et al., 2018). In this
151 case an area of 19×19 SEVIRI pixels and ARPA database were used respectively. This method is
152 based on the assumption that the plume is opaque and in thermal equilibrium with its environment.

153 2.2 Model simulations of plume dispersion and impacts

154 2.2.1 Plume dispersion with the FLEXPART Lagrangian model

155 We simulate the dispersion of the SO₂ plumes emanated by the Mount Etna activity during the
156 period 21-26/02/2021 using the Lagrangian dispersion model FLEXPART (Pisso et al., 2019). The
157 simulations are initialized with the emission rates and altitude estimated with SEVIRI, using the
158 methods described in Sect. 2.1. As meteorological inputs, our FLEXPART simulations use

159 European Centre for Medium-Range Weather Forecasts (ECMWF) ERA-5 reanalysis data at 30
160 km horizontal resolution and 137 height levels (100–200 m vertical resolution in the troposphere,
161 1–2 km in the lower stratosphere). The FLEXPART outputs are averaged over 30 min intervals
162 and are given at $0.1^\circ \times 0.1^\circ$ horizontal grid and 9 altitude levels, from the surface to 13 km altitude,
163 with a vertical resolution of 1 km, from 5 to 13 km, and a unique vertically-broad layer, from
164 surface to 5 km. Dry and wet deposition, as well as chemical depletion, are considered in the
165 simulations, using the default FLEXPART sink parameterization for SO₂.

166 2.2.2 Plume radiative forcing estimations with the UVSPEC radiative transfer model

167 We estimate the radiative impact of the Mount Etna plumes for the events under investigation
168 using the radiative transfer model UVSPEC and the LibRadtran package (Emde et al., 2016). The
169 equinox-equivalent clear-sky daily-average shortwave (integrated between 300 and 3000 nm)
170 surface and top of the atmosphere (TOA) direct radiative forcings (RF) are estimated with a similar
171 methodology as done by Sellitto et al. (2016, 2020); please refer to these previous works for more
172 details on the setup of the radiative model.

173 The background atmospheric state is set using the AFGL (Air Force Geophysics Laboratory)
174 winter mid-latitudes climatological standard. The surface albedo is set to 0.15, independent from
175 wavelength, which is a typical average shortwave albedo for the vegetated surfaces underlying the
176 locations associated with our study. Baseline and volcanically-perturbed radiative transfer
177 calculations are carried out using different aerosol layers configurations: using aerosol extinction
178 profiles at downwind LiDAR stations, as volcanically-perturbed conditions, and with the same
179 aerosol extinction profiles with the identified volcanic plume layer removed, as non-volcanic
180 baseline (see specific configurations in Sec. 4.5). Different hypotheses must be considered for the
181 non-measured optical parameters of volcanic aerosols. The spectral variability of the volcanic
182 aerosol extinction, the single scattering albedo and the angular distribution of the scattered
183 radiation are not directly measured and can be quite uncertain due to the possible presence of both
184 SA and a fraction of residual ash. Values of the Ångström exponent (a compact measure of the
185 spectral variability of the particle extinction and linked to the average size of the particles in the
186 plume), of the single scattering albedo (linked to the absorption properties of the aerosol layer)
187 and of the asymmetry parameter (linked to the angular distribution of the aerosol layer) are selected
188 for each case described in Sect. 4.5; please refer to this section for the details of these different
189 hypotheses. Different runs are realized, for all experiment, for different solar zenith angles (SZA)
190 to sample the full day. The daily-average shortwave TOA RF for the volcanically-perturbed
191 aerosol layer is calculated as the SZA-averaged upward diffuse irradiance for the baseline
192 simulation minus the volcanically-perturbed run, integrated over the whole shortwave spectral
193 range. The shortwave surface radiative forcing is calculated as the SZA-average downward global
194 (direct plus diffuse) irradiance for the volcanically-perturbed run minus the baseline, integrated
195 over the whole spectral range.

196 2.3 Satellite Observations of volcanic plumes

197 2.3.1 SO₂, SA and dust observations with IASI

198 The Infrared Atmospheric Sounder Interferometer (IASI) is a Fourier transform spectrometer
199 covering the large infrared spectral range between 645 and 2760 cm^{-1} , with a relatively high
200 spectral resolution (0.5 cm^{-1}) and a relatively small radiometric noise (noise equivalent spectral
201 radiance of about $20 \text{ mW}/(\text{cm}^{-1}\text{m}^2\text{sr})$ around 1000 cm^{-1}). The IASI instrument observes the Earth's

202 atmosphere and surface with a downward-looking geometry, with circular footprints of down to
203 12 km radius at the nadir spaced by 25 km, and with a swath of 2200 km (Clerbaux et al., 2009).
204 The instrument series are on board MetOp-A -B and -C spacecrafts since 2006, 2012 and 2018,
205 respectively. Each instrument of the series provides a near-global coverage every 12 h. For this
206 work, we have used IASI observations of SO₂, SA and dust.

207 The IASI daily SO₂ dataset includes SO₂ columns and volcanic plume altitude. The SO₂ partial
208 columns at 6 altitude intervals between 5 and 25 km are retrieved from IASI observations by
209 exploiting the correlation between brightness temperature differences and SO₂ total columns with
210 assumptions on the SO₂ plume altitudes (Clarisse et al., 2012). From these partial columns
211 profiles, the total column is obtained by vertical integration. In addition, the altitude of the SO₂
212 plume is estimated by using a sensitive trace gas detection method for high spectral infrared
213 measurements (Clarisse et al., 2014).

214 The detection of SA and its aerosol-type-specific optical depth is provided by the AEROIASI-
215 H₂SO₄ retrieval algorithm (Guermazi et al., 2021). The AEROIASI-H₂SO₄ algorithm is based on
216 a self-adapting Tikhonov-Phillips regularization method, built around the radiative transfer model
217 Karlsruhe Optimized and Precise Radiative transfer Algorithm (KOPRA) (Stiller et al., 2000). This
218 method iteratively fits each IASI spectrum at 20 spectral micro-windows by adjusting the vertical
219 profile of SA number concentration, jointly with water vapour profiles and surface temperature.
220 The SA are assumed as spherical droplets of an aqueous solution of sulphuric acid (H₂SO₄), and
221 the corresponding refractive indices are taken from Biermann et al. (2000). The information on the
222 total SA-specific optical depth is mainly provided by the selective absorption of the undissociated
223 H₂SO₄ in the SA solution droplets. The interference of the co-existent SO₂ is avoided by using
224 an operational spectral micro-window around 900 cm⁻¹, a spectral region characterised by H₂SO₄
225 absorption bands but outside the main SO₂-sensitive region around 1100-1200 cm⁻¹.

226 For the characterization of the three-dimensional distribution of desert dust plumes during the
227 event analyzed in the paper, we use the AEROIASI-Dust approach (Cuesta et al., 2015, 2020). The
228 AEROIASI-Dust algorithm derives vertical profiles of desert dust, in terms of extinction
229 coefficient at 10 μm, from individual thermal infrared spectra measured by IASI satellite sensor in
230 cloud-free conditions, both over land and ocean. This method iteratively fits each IASI spectrum
231 at 12 spectral micro-windows by adjusting the vertical profile of dust aerosol abundance jointly
232 with surface temperature. The information on the vertical distribution of dust is mainly provided
233 by their broadband radiative effect, which includes aerosol thermal emission depending at each
234 altitude on the vertical profile of temperature. As for AEROIASI-H₂SO₄, the AEROIASI-Dust
235 algorithm uses the radiative transfer model Karlsruhe Optimized and Precise Radiative transfer
236 Algorithm (KOPRA) (Stiller et al., 2000). The current paper uses AEROIASI retrievals from
237 version described by Cuesta et al., (2020) but using a complex refractive index derived by Di
238 Biagio et al. (2017) with a dust sample from a desert in Mali (which shows a smaller difference
239 between IASI and simulated spectra than that used by Cuesta et al. (2020)).

240 2.3.2 SO₂ and AI observations with Sentinel-5p TROPOMI

241 The TROPOspheric Monitoring Instrument (TROPOMI), onboard the Copernicus Sentinel 5
242 Precursor (S5p) spacecraft, is a joint project of the Netherlands Space Office and the European
243 Space Agency (Veefkind et al., 2012). The TROPOMI is a satellite-based spectrometer operating
244 in the ultraviolet/visible/near infrared spectral region and at a nadir-viewing geometry. It provides
245 observation of key atmospheric constituents at the unprecedented high spatial resolution of down

246 to $7 \times 3.5 \text{ km}^2$. In the present work, we use the offline Level 2 datasets of Aerosol Absorbing Index
247 and the total SO₂ column.

248 The UltraViolet Aerosol Absorbing Index (UVAI) is a compact parameter used to visualize the
249 presence of absorbing aerosols in the sampled airmasses. It is based on the spectral ratio of the
250 measured top of the atmosphere reflectance and a pre-calculated theoretical reflectance for a
251 Rayleigh scattering-only atmosphere, at a given pair of UV wavelength. Positive residuals of the
252 observed and modelled reflectances are linked to the presence of UV-absorbing aerosols, like dust
253 and smoke. Negative residuals may indicate the presence of non-absorbing aerosols, while values
254 close to zero are found in the presence of clouds or no aerosols. As the UVAI is dependent on
255 different aerosol layer optical and morphological properties, and on the underlying surface
256 reflectance, in this paper we use this parameter only as a general indication of the presence of dust.
257 The total column SO₂ is retrieved using a DOAS (Differential Optical Absorption Spectroscopy)
258 method. The SO₂ slant column density (SCD), i.e. the SO₂ concentration along the mean light
259 path through the atmosphere, is derived by fitting cross-sections in a spectral range characterised
260 by the absorption of SO₂ (in this case, at different spectral fitting micro-window between 310 and
261 390 nm, depending on the SO₂ burden). After different calibrations and corrections of the derived
262 SO₂ SCD, this latter is converted to vertical columns using the air mass factor from radiative
263 transfer calculations. For more details about the TROPOMI total column SO₂ product, please refer
264 to Theys et al. (2017).

265 2.3.3 SO₂ observations with OMPS-NM

266 The Ozone Mapping and Profiler Suite Nadir Mapper (OMPS-NM) flies on the Suomi National
267 Polar-orbiting Partnership (Suomi-NPP) satellite since 2012 and measures the Earth backscattered
268 UV/visible radiation at a nadir-viewing geometry (Ditman et al., 2002). In this work, the Level 2
269 height-resolved SO₂ product is used. For this product, a direct vertical column fitting algorithm is
270 used to retrieve the SO₂ column amounts in the lower (centered at 2.5 km), middle (centered at
271 7.5 km) and upper (centered at 11 km) troposphere, as well as the lower stratosphere (centered at
272 16 km).

273 2.3.3 Aerosol classification with CALIOP

274 The Cloud-Aerosol Lidar with Orthogonal Polarization (CALIOP) is a LiDAR system onboard
275 the Cloud-Aerosol Lidar and Infrared Pathfinder Satellite Observation (CALIPSO) spacecraft ; it
276 flies at about 700 km altitude in a sun-synchronous orbit and is part of the so-called A-Train
277 (Winker et al., 2010). The CALIOP space LiDAR is in orbit since April 2006 and is still in
278 operation. It provides vertical profiles of aerosols and clouds at about 01:30 and 13:30 local time.
279 In this work, we use aerosol detections of the Vertical Feature Mask level 2 product version 4.2,
280 at varying horizontal resolution, as well as the related aerosol types classification information.

281 2.4 Ground-based observations

282 2.4.1 MPLNET LiDAR observations at Sede Boker site

283 The National Aeronautics and Space Administration (NASA) Micropulse Lidar Network
284 (MPLNET; Welton et al., 2001) project was established in 1999 in support of the NASA Earth
285 Observing System (EOS; Wielicki et al., 1995). During the last two decades, MPLNET
286 observations have significantly contributed to fundamental studies and applications on climate

287 change and air quality studies and in support for NASA satellite and sub-orbital missions (Lolli et
288 al., 2018, Bilal et al., 2019, Lolli et al., 2020, Lewis et al., 2020, Campbell et al., 2021). This
289 federated global network is constituted by homogeneous commercially available Micropulse
290 LiDARs (MPL) instruments manufactured by Droplet Measurement Technology. The MPLNET
291 instruments are single-wavelength LiDAR systems that use a diode-pumped Nd:Yag laser at 532
292 nm, with a 1-minute temporal resolution and 75-meter vertical resolution. The MPLNET network
293 is active during the whole day and night and operates in all weather conditions, in the limit of laser
294 signal extinction. The MPLNET network is deployed at global scale and cover all latitudes bands.
295 For this study, the observations from Sede Boker (30.8° N, 34.8° E, 480 m a.s.l.) permanent
296 MPLNET site are specifically used. To retrieve the vertically-resolved optical aerosol and cloud
297 properties from a single wavelength LiDAR, strong assumptions, that limit retrieval accuracy, are
298 needed. To reduce this uncertainty, MPLNET LiDAR network deploys the instruments, if possible,
299 together with an Aerosol Robotic Network (AERONET; Holben et al., 1998) sun-photometer to
300 constrain the LiDAR equation and reduce the retrieval errors (Welton et al, 2000). More details on
301 the full MPLNET standard data product suite, including aerosols, have been provided by Welton
302 et al. (2018). The standard, automated, MPLNET products are not designed to accurately capture
303 elevated volcanic plumes due to their transient nature, high altitude, and unique microphysical
304 properties relative to the local aerosols that limit the usefulness of the constrained aerosol retrieval
305 approach. Instead, MPLNET provides a custom retrieval method that bypasses the automated
306 aerosol height algorithm, and requires manual specification of the plume altitude (for this study
307 based on inspection of the lidar signal and volume depolarization ratio profiles). Upon
308 specification of the plume base and top, the optical depth of the plume is determined using the
309 attenuation of the lidar signal and a molecular scattering (Lewis et al, 2016). The retrieval of plume
310 properties is calculated using the same MPLNET constrained retrieval algorithm using the plume
311 optical depth. This process often results in few retrievals during the plume's advection over the
312 lidar site as calculation of the plume optical depth is difficult with noisy signals. Instead, the Lidar
313 Ratios from these few retrievals are averaged, and the result is used to determine the plume
314 properties by fixing the Lidar Ratio using the classic Fernald lidar algorithm (Fernald 1984). The
315 retrieved lidar ratios were in good agreement with several LiDAR studies on volcanic emissions
316 (e.g., Prata et al., 2017) and a fixed value of 50 sr was used. Data is freely available on MPLNET
317 website (<https://mplnet.gsfc.nasa.gov/>).

318 2.4.2 The ACTRIS-Fr OHP LiDAR Observatory

319 The Observatoire de Haute-Provence (OHP) located in southern France (43.9° N, 5.7° E, 670 m
320 a.s.l.) is one of the NDACC (Network for the Detection of Atmospheric Composition Change)
321 alpine stations, equipped with a variety of LiDAR instruments for monitoring of the lower and
322 middle atmosphere.

323 The longest continuous LiDAR data record at OHP is provided by a Rayleigh-Mie-Raman LiDAR
324 for temperature and aerosol measurements (hereafter referred to as LTA) operating at the
325 wavelength of 532 nm. The LTA instrument (Keckhut et al., 1993) has provided routine
326 measurements for over 3 decades with a mean measurement rate of 10-12 nighttime acquisition
327 nights per month and a typical duration of acquisition of 3-5 hours. To retrieve the vertical profiles
328 of aerosol backscatter and extinction, the raw lidar returns from three LTA elastic channels,
329 covering respectively troposphere, lower stratosphere and upper stratosphere, are merged and a
330 Fernald-Klett inversion method is applied (Fernald, 1984), assuming a constant LiDAR ratio of 50
331 sr. The retrieved backscatter and extinction coefficients are reported with a time resolution of 1

332 minute and a vertical resolution of 15 m. The scattering ratio is then computed as a ratio of total
333 (molecular plus aerosol) to molecular backscattering, where the latter is derived from ECMWF
334 meteorological data. A more detailed description of the instrument, aerosol retrieval and error
335 budget is provided by Khaykin et al. (2017) and references therein.

336 The ultraviolet tropospheric differential absorption LiDAR (LiO3tr) also operated at OHP at the
337 same time as the LTA LiDAR. It records backscatter signal at 316 nm for ozone monitoring
338 (Ancellet et al. 1997, Gaudel et al. 2015). The 316 nm signal is very weakly absorbed by ozone in
339 the troposphere and can be used for aerosol backscatter monitoring between 3 and 13 km altitude.
340 As for the LTA instrument, the Fernald-Klett inversion method (Fernald, 1984) is applied
341 assuming a constant LiDAR ratio of 50 sr at 316 nm and a 1.01 scattering ratio close to a molecular
342 return at 11 km. Since no overlap correction is applied in order to match the LTA retrieval at 3
343 km, a scattering ratio uncertainty of the order of 10% is expected below 4 km.

344 The OHP observatory is also equipped with an automatic LiDAR (CIMEL model CE376)
345 sounding in the troposphere from ~200 m to ~12 km of altitude at the wavelength of 532 nm,
346 named GAIA and operational since 2019. The GAIA system is also equipped with a depolarization
347 channel at the same wavelength to gather more information on the nature and optical properties of
348 aerosols, mostly in the boundary layer and in the free troposphere. It provides data at a frequency
349 of 1 mn and the datasets are then averaged on 10 min slices. Its spatial resolution is 15 m. The
350 scattering ratio is computed as for the LTA LiDAR, but interpolating radiosoundings collected at
351 OHP launched every week in the late morning. The data are corrected for instrumental deadtime,
352 overlap in the first hundreds of meters of altitude (using an algorithm called CHECK delivered by
353 the PHOTONS-AERONET network), sky background and squared altitude to take into account
354 the quadratic decrease of the signal in function of altitude. A Haar wavelet method (Brooks 2003,
355 Cohn and Angevine 2000) can then be used to retrieve the boundary layer height. The GAIA data
356 are inverted using the Klett method (Klett 1981).

357

358 2.4.3 The ACTRIS Napoli LiDAR observatory

359 The Napoli LiDAR observatory (Naples, Italy, 4.18° E, 40.84° N, 118 m a.s.l.) is part of the
360 ACTRIS (Aerosol, Clouds and Trace Gases Research Infrastructure) research infrastructure, a pan-
361 European distributed research infrastructure for short-lived atmospheric constituents producing
362 high-quality data in the area of atmospheric science (Wandinger et al., 2020). The Napoli
363 observatory includes passive and active remote sensing systems and near-surface sampling
364 systems, for atmospheric studies. Thanks to its quite central location in the Mediterranean basin,
365 it represents a strategic location to study optical and microphysical properties of the aerosols
366 coming from local sources and long-range transport.

367 The station is equipped with a multiwavelength elastic/Raman LiDAR device able to detect elastic
368 signals at 355 nm, 532 nm and 1064 nm, Raman N₂ echoes at 386 nm and 607 nm and aerosol
369 depolarization at 532 nm. Details on this LiDAR system are reported by Boselli et al. (2021).
370 Vertical profiles of the aerosol extinction coefficient and linear depolarization ratio are shown and
371 discussed in this paper. The aerosol extinction coefficient profiles were retrieved using the
372 procedure introduced by Ansmann et al (1990). The calibrated particles linear depolarization
373 profiles were obtained from the backscattered light polarized along both perpendicular and parallel

374 directions respect to the laser beam polarization and following the inversion procedure reported
375 by Biele et al. (2000) and Freudenthaler et al., (2006).

376 2.4.3 The AERONET observations

377 Total column measurements of the aerosol optical depth (AOD), Ångström exponent and single
378 scattering albedo at several wavelengths, among others aerosol parameters, are carried out globally
379 with Cimel sun photometers, as part of the AEROSOL ROBOTIC NETWORK (AERONET; see the
380 AERONET website at <http://aeronet.gsfc.nasa.gov> and the description by Holben et al., 1998, for
381 further details). In this manuscript we use the AERONET observations for these three aerosol
382 parameters at the selected station of Sede Boker, OHP and Napoli, which are part of the
383 AERONET network.

384 **3 The Mount Etna activity in February and March 2021**

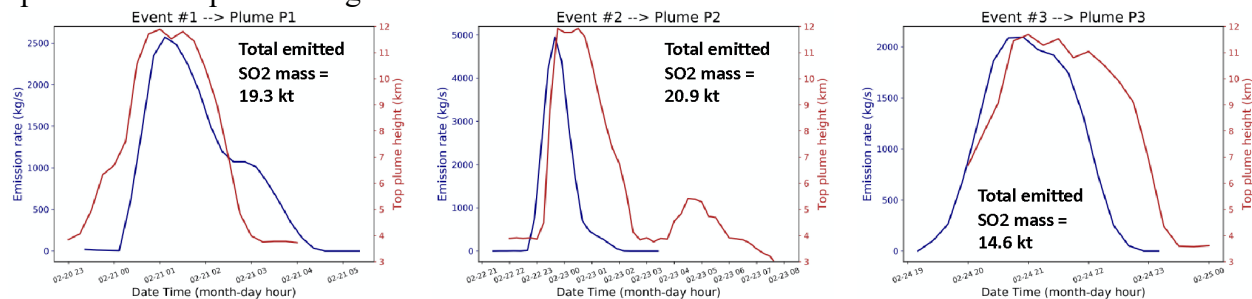
385 Between February and April 2021, Mount Etna experienced an intense eruptive activity from the
386 South East Crater (SEC) consisting of astonishing short-lasting lava fountain eruptions coupled
387 with lava effusion and episodic pyroclastic density currents. The activity took place while all the
388 summit craters, Bocca Nuova, Voragine, North-East crater, were displaying a mild strombolian
389 activity and lava effusion at Voragine and Bocca Nuova craters continuously since September
390 2019. Differently than the other three summit craters, over the same period SEC was episodically
391 erupting but featured a slow and gradual energy increase of its eruptive activity. Eruption,
392 eventually intensified between December 2020 and January 2021 to abruptly escalate on the
393 afternoon of 16 February 2021, starting to produce a sequence of lava fountaining which ended on
394 1st April 2021. Over these two months, 17 paroxysmal episodes were produced with a recurrent
395 characterisation, consisting of the resumption of strombolian activity growing in intensity, lava
396 flow effusion, and transition from discrete explosions to the continuous gas and lava jetting typical
397 of lava fountaining. Overall, each lava fountain lasts few hours while producing the sudden
398 spreading in the atmosphere of a volcanic ash and SO₂ plume that rose for a mean altitude of 10
399 km asl. Each eruptive episode was accompanied by the dispersal of ash plumes and fall-out
400 deposits in the surrounding towns of the volcano up to Catania, which often pose severe hazards
401 to aviation and repeated temporary closures of the Catania international airport. Lava flows
402 propagated mostly in the eastern flank of the volcano in the Valle del Bove and remained confined
403 at a mean altitude of 2,700 m asl. In the present study we focus on the specific phase, during this
404 broad activity, occurring between the 21 and 26/02/2021. Three main short-lived paroxysmal
405 events, discussed in Sec. 4.1, occurred during this time period.

406 **4 Results**

407 4.1 Three paroxysms in four days: the SO₂ emissions

408 The method described in Sect. 2.1 was applied to the SEVIRI observations of 21-26/02/2021 to
409 estimate the SO₂ emission rate and altitude of plume injection for the three individual paroxysms
410 in this timeframe. In Fig. 1, the temporal profile of the emission rate and altitude, for the Events
411 #1, 2 and 3 (whose dispersion is subsequently associated to the three plumes referred to as plumes
412 P1, P2 and P3 in Sect. 4.2) are shown. The SO₂ emissions associated to the Event #1 started at
413 about 23:00 of 20/02 and sharply increased during the first hours of the day 21/02. The emission
414 rate for this event peaked at values of about 2000-2500 kg s⁻¹ at 01:00 to 02:00 of 21/02. During

415 this event, the injection altitude is also sharply increasing from the crater altitude to about 12 km,
 416 peaking between 01:00 and 02:00 of 21/02. The SO₂ emissions for the Event #1 sharply decreased
 417 afterwards and the paroxysm was over by about 04:00 of 21/02. The Event #2 started at about the
 418 same time but one day later than Event #1. The Event #2 had a sensibly shorter duration than Event
 419 #1 - it started at about 23:00 of 21/02 and was over by 01:00 of 22/02 - but its peak emission rate
 420 is nearly twice as large than for the Event #1, peaking at about 5000 kg s⁻¹ on 22/02 00:00. The
 421 injection altitude for the Event #2 peaks at 12 km, in a similar fashion as the Event #1. At about
 422 19:00 of 24/02, the Event #3 kicked off. The temporal profile and duration of the SO₂ emission
 423 rate and injection altitude for the Event #3 is similar to those of the Event #1, with a slightly smaller
 424 peak value of the emission rate (1500-2000 between 20:00 and 22:00 of 24/02).
 425 The total emitted SO₂ mass for the three events has been estimated at values of 19.3, 20.9 and 14.6
 426 kt for the Event #1, 2 and 3, respectively. The Event #2 injected the largest amount of SO₂, despite
 427 the shortest duration for the ensemble of the three events, due to the significantly larger peak
 428 emission rate. The total SO₂ mass emitted from the three added events is 55 kt. Typical values of
 429 the emission rates for moderate-to-strong eruption of Mount Etna are generally less than
 430 2000 kg s⁻¹ (Sellitto et al., 2016, Corradini et al., 2020). This specific activity is then characterised
 431 by relatively brief but very intense paroxysmal events, if compared to more general behaviour of
 432 Mount Etna. In addition, the altitude of the plume injection is particularly high. Documented
 433 extremely high-altitude eruptions of Mount Etna rarely exceed 10-11 km altitude (e.g. Sellitto et
 434 al., 2016, Corradini et al., 2020). Thus, this series of three paroxysms qualify as an extreme event
 435 in terms of the injection altitude. The total SO₂ mass emitted during these few days of activity is
 436 about 50% of the record-breaking sequence of eruptions of 24-31/02/2015, which was estimated,
 437 with a similar method as the present paper, at about 100.0 kt overall (Corradini et al., 2020). Thus,
 438 in terms of the SO₂ emission rates and injection altitude, as well as for its total SO₂ emitted mass,
 439 the sequence of three events during 21-26/02/2021 has to be categorised as one in the higher
 440 spectrum of eruption strengths of Mount Etna.



441
 442 *Figure 1: Temporal profile of the emission rates (blue lines) and injection altitude (red lines) for the three paroxysmal events*
 443 *(Event #1-3 in the figure) of Mount Etna in the period 21-26/02/2021. The total emitted SO₂ mass, for each of the three events, is*
 444 *also reported in the individual panels.*

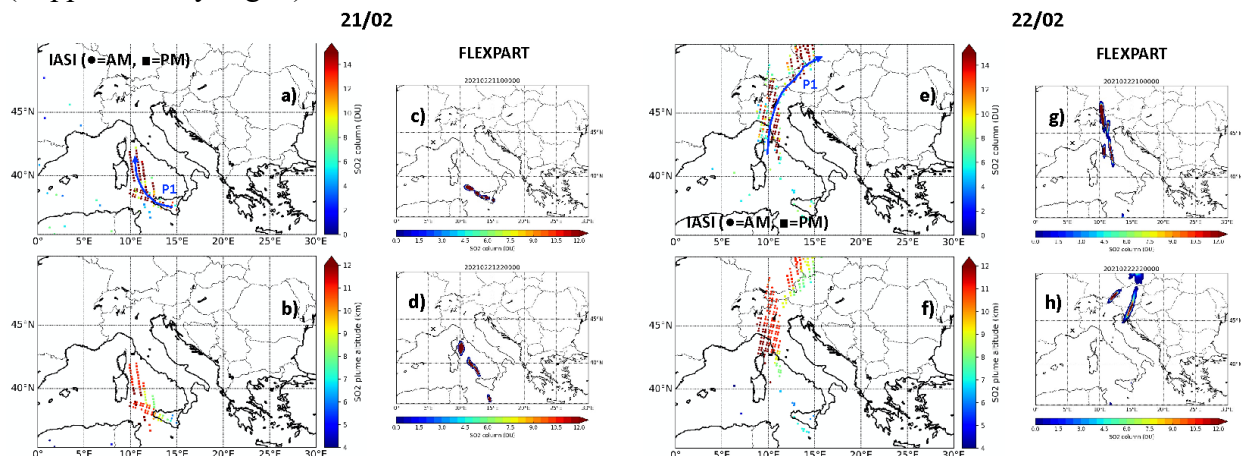
445 4.2 An uncommon transport toward the north: the SO₂ plume dispersion

446 The plumes emanating from the three individual paroxysmal events described in the previous
 447 section are then characterised in terms of their subsequent dispersion.
 448 Figures 2-4 show the SO₂ column amount and plume altitude obtained from IASI observations,
 449 and the SO₂ column amount obtained from FLEXPART simulations, for 21-22 (Fig. 2), 23-24
 450 (Fig. 3) and 25-26/02 (Fig. 4). The FLEXPART SO₂ simulations are obtained using the measured
 451 SO₂ emissions described in Sect. 4.1. As extensively discussed by Sellitto et al. (2016), the
 452 synergy of good quality regional observations from satellite and realistic simulations is crucial to
 453 get more comprehensive insight into confined plumes dispersion, thanks to the information

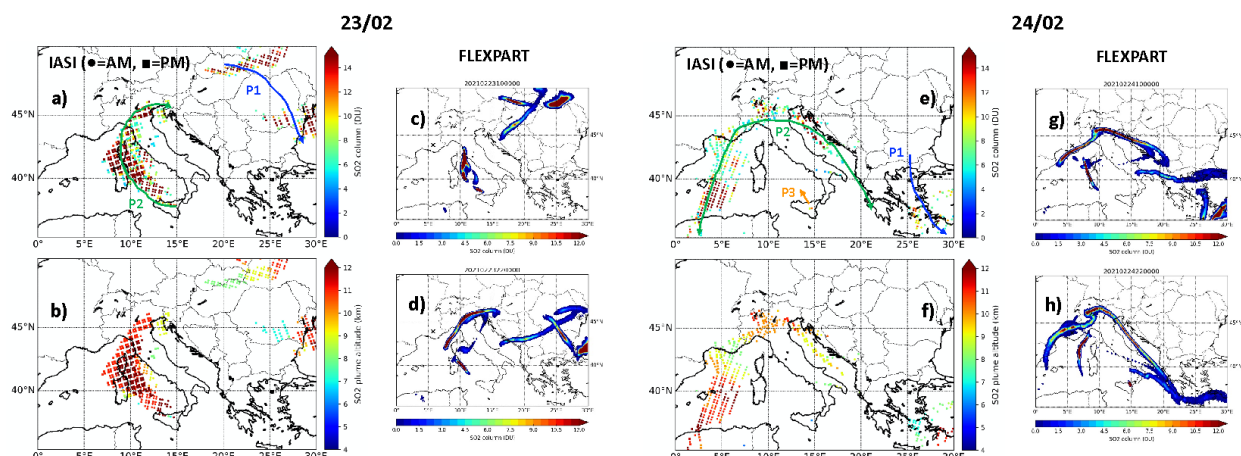
454 complementarity of these two information layers. In fact, the vertical sensitivity of satellite
455 observations of SO₂ is limited, thus satellite observations can only provide a partial information
456 on the height distribution of SO₂; on the other hand, uncertainties in the input parameters and the
457 physico-chemical in-plume processes can impact on the realism of dispersion simulations. In
458 addition, the temporal sampling of satellite observations, one or two overpasses per day for low-
459 Earth orbit spacecraft, is usually not sufficient to smoothly characterise the temporal evolution of
460 the plume's dispersion. On the contrary, dispersion simulations can be realised at sub-hour
461 temporal resolution, thus filling the temporal gap between satellite overpasses. An animation of
462 the FLEXPART simulations for this case study, with the full temporal resolution of 30 minutes,
463 can be found as Supplement. As it is possible to notice from Figs. 2-4, the description of the plume
464 dispersion with observations and simulations is very consistent, thus cementing our confidence in
465 our further interpretation of the plumes dynamics.

466 On 21/02, the plume P1, linked to the paroxysmal Event #1, disperses towards the central
467 Tyrrhenian Sea, reaching Corsica to the western coast of Tuscany, for the night overpass of IASI
468 (about 21:30 LT). During this phase, the plume stayed between 10-12 km altitude, with lower-
469 altitude sections at the southern end of the plume. Values slightly higher than 15 DU are found for
470 plume P1 during this phase, both from observations and modelling. The plume P1 then dispersed
471 towards more north-eastern direction on the 22/02, to northern Italy and then Austria and further
472 north-east, while progressively slightly descending at lower altitudes (down to 8-10 km). Clusters
473 of relatively large values of the SO₂ column, around 15 DU, are found on 22/02. Plume P1
474 orientates around an anticyclonic circulation due to the presence of a stable Omega block in Central
475 Europe (Hoshyaripour, 2021), dispersing towards the south-eastern direction on 23/02 and then
476 disperses further east, reaching Turkey and the Middle East on 24/02. The SO₂ column
477 concentration for P1 remained relatively large, with values larger than 10 DU, while the plume
478 kept descending, down to 7-10 km on 24/02. On 23/02, plume P2 (linked to the paroxysmal Event
479 #2) kicked off with a similar initial dispersion as for P1, towards the central Tyrrhenian Sea, before
480 starting to spread on 23/02 afternoon, from southern France to the Adriatic Sea. By 24/02, the
481 plume P2 has formed an elongated and almost filamentary shape of quite large horizontal extent,
482 from northern Spain, to the west, to southern Greece, to the east. Plume P2 was also much more
483 irregular, in terms of both SO₂ column amount and plume altitude than plume P1. Values as high
484 as 15 DU are found at the western and eastern ends of the plume, with mean altitudes at about 9 to
485 12 km. Smaller column values, around 5-6 DU, and a mean altitude of about 10 km are found in
486 the central area of the plume, in sub-alpine northern Italy. Plume P2 then compressed (i.e. the
487 western and eastern ends of the plume got closer) on 25/02 and formed a curly plume then starting
488 to disperse towards the north-east on 26/02. During this phase, the eastern end of plume P2 swept
489 through southern Italy, still keeping at 8-9 km altitude. Plume P3 (linked to the paroxysmal Event
490 #3) appears on 25/02 morning, again orientating towards the central Tyrrhenian Sea, while rapidly
491 dispersing towards the east together with plume P2. Plume P3 displayed slightly larger values of
492 the SO₂ column (larger than 15-18 DU) and lower altitude (7-10 km) than plumes P1 and P2. This
493 overall description of the dispersion of the plumes P1-3 in the upper-troposphere (UT) is confirmed

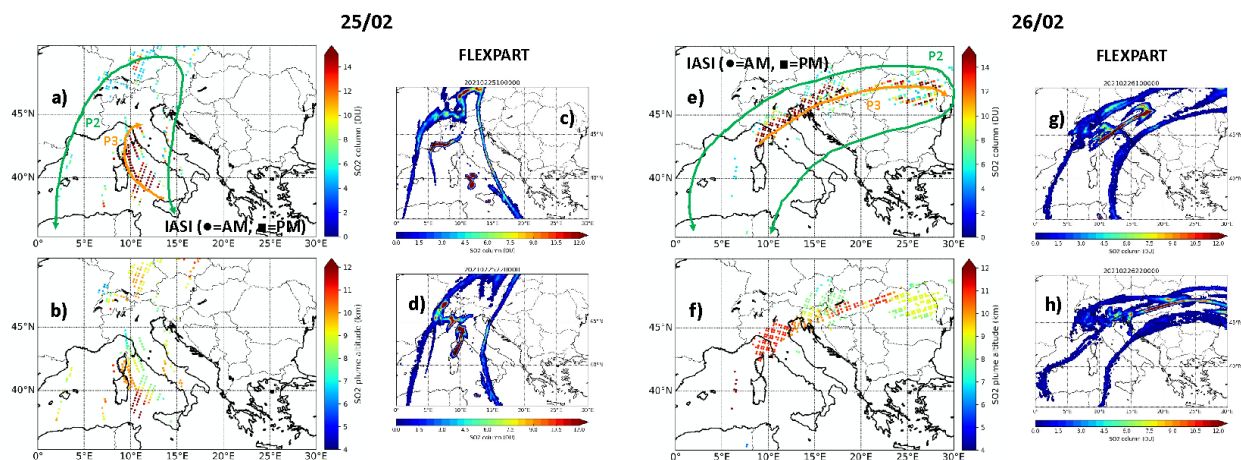
494 by the independent observations of the upper-tropospheric SO₂ column from OMPS-NM
 495 (Supplementary Fig. 1).



496
 497
 498
 499
 500
 Figure 2: IASI SO₂ column (a,e) and mean altitude of the plume (b,f) for the morning (approximate overpass at ~9:30 LT, circles) and afternoon (approximate overpass at ~21:30 LT, squares) MetOp-A spacecraft overpass; corresponding FLEXPART SO₂ column simulations (at 10:00 LT, c,g, and at 22:00 LT, d,h), for 21 and 22/02/2021. Plume P1 is individuated, and its approximate direction of dispersion is indicated as a blue arrow in panels a and e.



501
 502
 503
 Figure 3: same as Figure 2 but for 23 and 24/02/2021. Plumes P1, P2 and P3 are individuated, and their approximate directions of dispersion are indicated as blue, green and orange arrows, respectively, in panels a and e.



504
 505
 506
 Figure 4: same as Figure 2 but for 25 and 26/02/2021. Plumes P2 and P3 are individuated, and their approximate directions of dispersion are indicated as green and orange arrows, respectively, in panels a and e.

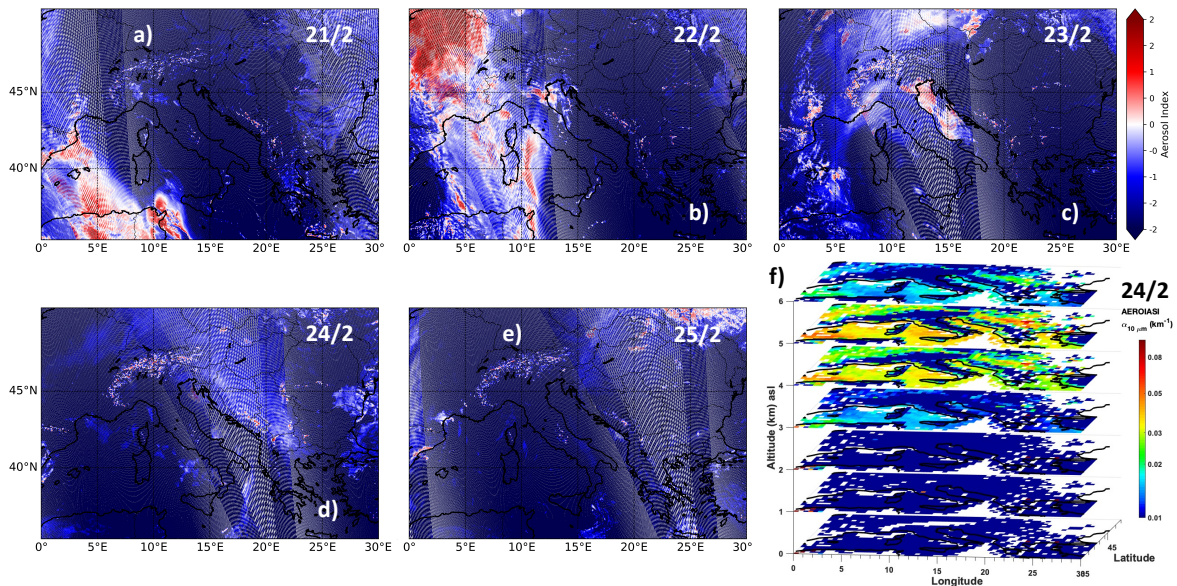
507 More in general, the dispersion of plumes P1-3 was consistently directed towards the northern
508 quadrant from the perspective of the Mount Etna volcanic source. Using a more-than-one-decade
509 long dispersion simulations dataset, Sellitto et al. (2017) have estimated the prevalent direction of
510 dispersion of the plumes generated from Mount Etna emissions. They have found that for more
511 than 80% of the time Mount Etna's plumes disperse towards the eastern quadrant. The dispersion
512 towards the northern and north-western quadrant, as is the case for the initial dispersion for these
513 events, is a rare occurrence, accounting only for less than 5% of the cases. On the other hand, the
514 northern and north-western sectors are the only downwind areas that assure the presence of
515 continental long-term active observatories that can allow the downwind observation and
516 characterisation of Mount Etna's plumes. Thus, this series of paroxysms is a rare occasion to study
517 more in details the dispersed plume of Mount Etna's volcanic emissions.

518 4.3 Not only volcanic aerosols: the dust events of February 2021

519 During the same period of the series of volcanic events discussed in this manuscript, a major
520 Saharan dust outbreak to central Europe occurred (Hoshyariapour 2021). Starting from 21/02, a
521 trailing cold front produced a sustained dust uptake in northern Morocco and Algeria; the dust was
522 then transported towards western Europe by southerly flow, was lifted by warm conveyor belt, and
523 entered the mentioned Omega block located in central Europe, thus orienting in an anticyclonic
524 circulation similar to volcanic plume P1. More specific analysis of this dust event is beyond the
525 scopes of the present paper. Nevertheless, here we characterise the bulk dust distribution during
526 this event, so to help the interpretation of the volcanic plumes at downwind observatories of Sect.
527 4.4.

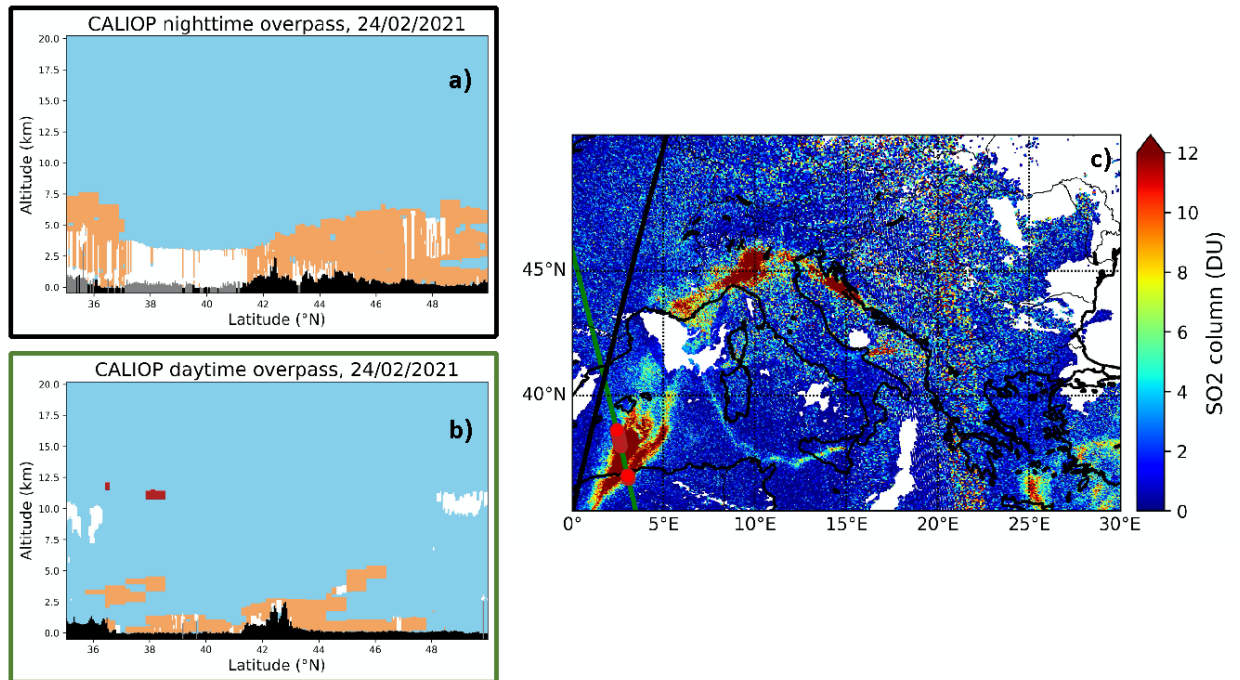
528 Figures 5a-e display the UVAI observations from TROPOMI during this period. They show the
529 dust emitted from north-western Sahara towards the Western Mediterranean and North-Eastern
530 Spain on 21/02, thus reaching Central and Northern France on 22/02 and then circulating around
531 the Omega block high pressure during the following days, with weaker and weaker UVAI
532 signature, possibly do to dust removal and dispersion. The vertical distribution of Saharan dust for
533 this event is further investigated using the height-resolved information of the AEROIASI-Dust
534 algorithm. In Fig. 5f, the dust-specific aerosol extinction profiles at 10 μm , from AEROIASI-Dust,

535 is shown for the 24/02. The dust looks confined, in the region of interest of our study, between 3
 536 and 6 km altitude.



537
 538 *Figure 5: UVAI retrievals with S5p TROPOMI for the period 21-25/02 (a,e). Dust-specific aerosol extinction at 10 μm from*
 539 *AEROSIAI-Dust observations for 24/02, from surface to 6 km altitudes (f).*

540 Figure 6a,b show the CALIOP feature layer classification for CALIOP day and night overpasses
 541 in the area of interest (see ground tracks of CALIOP in Fig. 6c), on 24/02. Both day and night
 542 overpasses confirm the presence of dust from near-surface to 5-7 km altitude. The lifting of the
 543 dust layer in the south-north direction, from North Africa to Central Europe, is clearly visible.
 544 Figure 6b also shows evidence of the volcanic plume from Mount Etna plume P2. As discussed
 545 more in details in Sect. 4.4, the plume P2 arrives in Southern France and Spain coastal areas on
 546 24/02 afternoon, which is consistent with the two CALIOP overpasses of Fig. 6a,b. An early
 547 observation of the plume P2 on 23/02, in the central Tyrrhenian Sea, together with the underlying
 548 dust layer, is shown in the Supplementary Fig. 2. The volcanic aerosol layer is reasonably co-
 549 located with the volcanic SO₂ plume, observed with TROPOMI, for both overpasses (23/02,
 550 Supplementary Fig. 2b, and 24/02, Fig. 6c). The volcanic plume P2 observed by CALIOP, is
 551 located at exceptionally high altitudes for Mount Etna's activity, at 12-13 km on the 23/02 and
 552 then slightly descending to 11-12 km on 24/02. The vertical plume location is very consistent with
 553 IASI observations and FLEXPART simulation of the SO₂ plume discussed in Sect. 4.2. The
 554 volcanic and the dust plumes remain completely vertically-separated in this area.



555

556 *Figure 6: (a,b) Feature layer classification (sky blue: clear sky, black: Earth's surface, white: clouds, brown: tropospheric*
 557 *aerosol – here classified as dust, red: stratospheric aerosol feature – here classified as volcanic, grey: no signal) for CALIOP*
 558 *nighttime, at ~2:00 am (a) and daytime, at ~1:30 pm (b), overpasses for 24/02/2021. (c) Sentinel-5p TROPOMI SO2 column*
 559 *observations for 24/02/2021. The black and green lines in panel c are the ground tracks of CALIOP observations of panel a*
 560 *and b, respectively. The position of the stratospheric aerosol (volcanic) feature, identified in panel b, is also indicated in panel c*
 561 *as red circles.*

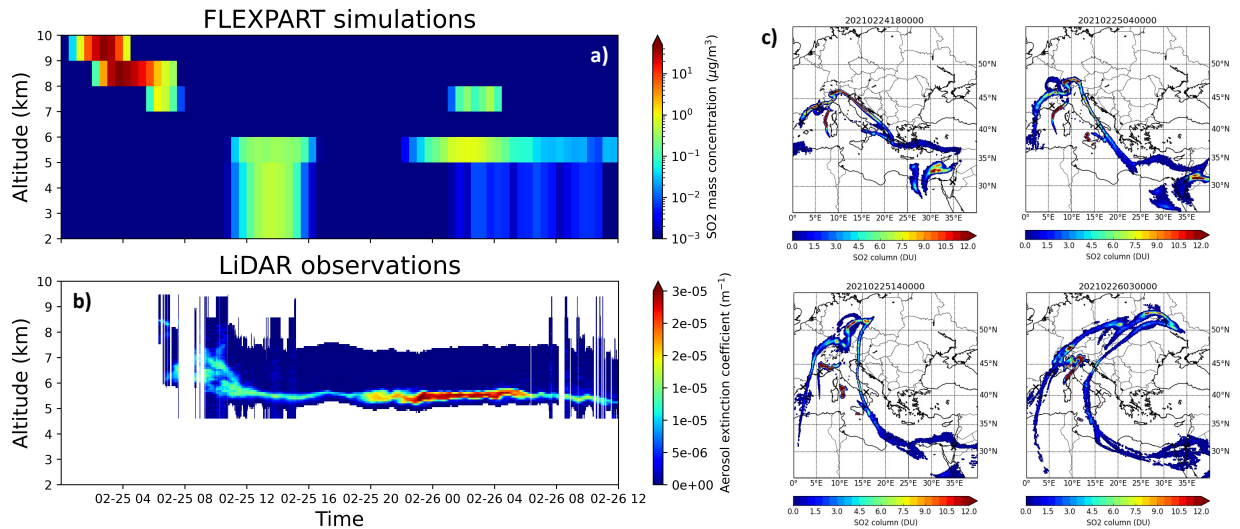
562 4.4 The volcanic plumes themselves: observations at downwind observatories

563 The uncommon transport of Mount Etna's plumes towards the north, for these three events, is a
 564 rare occasion to monitor and characterise the volcanic aerosols in Mount Etna's plumes at well-
 565 equipped observatories, including vertical information with LiDAR systems. As mentioned above,
 566 in the large majority of cases, Mount Etna's plumes disperse towards the east, in a mainly marine
 567 region where very few ground observation stations are present. On the contrary, there is significant
 568 density of ground stations northwards, i.e. in continental Europe.

569 Plumes P1 and P2 have been observed downwind at different stations. Here in the following, we
 570 analyse the plume's observations at three stations: Sede Boker, Israel, OHP, France, and Napoli,
 571 Italy.

572 Figure 7a shows the volcanic plume vertical distribution over Sede Boker station, in terms of the
 573 SO2 volcanic tracer, from FLEXPART simulations. Figure 7b shows the series of LiDAR aerosol
 574 observations at Sede Boker, for the same period. The plume P1, after a relatively long dispersion
 575 phase over central-easter Europe, driven by anticyclonic flow of the Omega block discussed in
 576 Sect. 4.2 (see Fig. 2 and 3, as well as the animation in the Supplementary material), overpasses the
 577 Sede Boker station starting from 25/02 early in the morning and, with discontinuous broken
 578 dispersed plumes sections, until 26/02 in the early afternoon, as visible from Fig. 7c. More dense
 579 clusters of the plume P1 overpass the station during the period spanning from 25/02 night to 26/02
 580 early morning. During this plume's overpass, P1 has aged 4-5 days since their volcanic emissions.
 581 The LiDAR observations show an aerosol layer linked to the plume P1 in the same period indicated
 582 by the FLEXPART simulations. Even if a part of the plume observation is missed by the LiDAR,

583 during the night between 24 and 25/02 (due to low LiDAR signal quality), a consistent vertical
 584 behaviour is shown by simulations and observations. Both information layers show an initially
 585 higher plume, located at 9-10 km, then descending to 5-6 km altitude. The plume looks
 586 filamentary, with a geometrical vertical thickness of less than 500 meters (Figs. 7a and b) and a
 587 horizontally-confined shape (Fig. 7c). The mean aerosol depolarization for the plume is $32.3 \pm 1.4\%$
 588 (Tab. 1). This value is very elevated for volcanic aerosols and might indicate the presence of a
 589 large fraction of fine ash, for plume P1. The three-dimensional morphology of this aerosol layer,
 590 as detected by LiDAR, as well as the consistency of observations with volcanic tracer dispersion
 591 simulations, suggest that a significant presence of dust can be excluded at these altitudes.



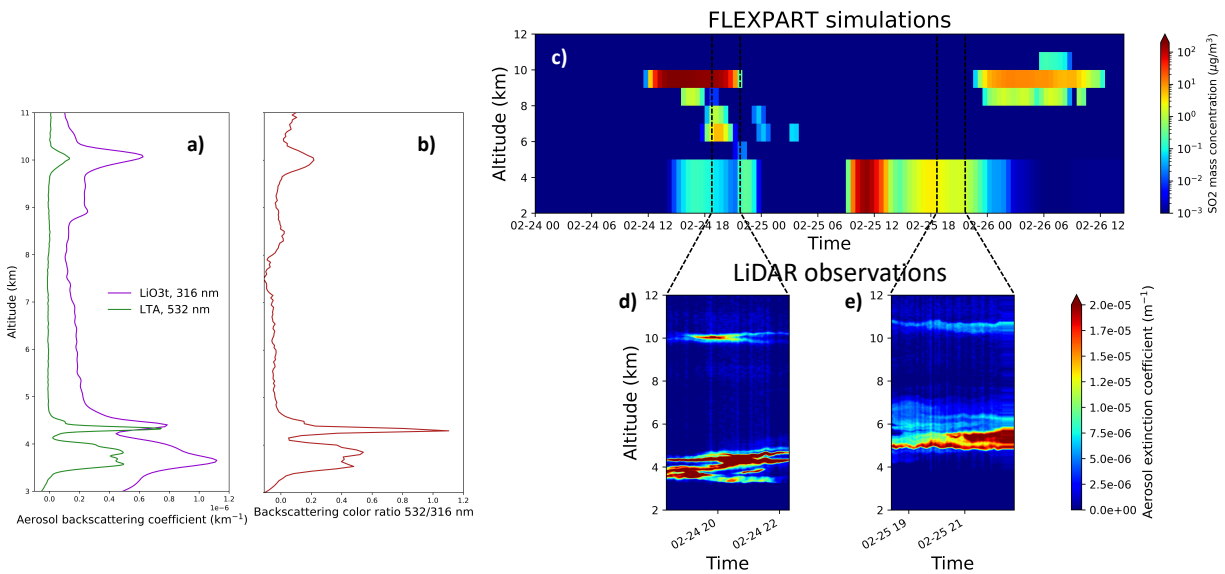
592

593 *Figure 7: FLEXPART SO₂ mass concentration profiles, from 25/02/2021 00:00 to 26/02/2021 12:00, over Sede Boker station (a).*
 594 *Volcanic-aerosol-specific LiDAR observations of the aerosol extinction coefficient, for the same period as in panel a, at Sede Boker*
 595 *station (b). Selected maps of the SO₂ total column dispersion, between 24/02 and 26/02/2021, from FLEXPART simulations (c).*
 596 *The position of the Sede Boker station is shown as a black cross in panel c.*

597 The western and eastern peripheries of the dispersed plume P2 (hereafter referred to as P2/W and
 598 P2/E, respectively) are almost synoptically observed at OHP (P2/W) and Napoli (PE/E) ground
 599 stations. Starting from 24/02, the plume P2 takes an elongated and then folded-shaped geometry,
 600 with the western periphery P2/W slowly moving south-westwards over Southern France and
 601 Eastern Spain, and the eastern periphery P2/E sweeping Southern Italy in a north-western direction
 602 (Fig. 3-4).

603 Basing on FLEXPART simulations, the P2/W section arrives at OHP station basically in two
 604 separate phases: during evening/night of 24/02 and during night/early morning between 25 and
 605 26/02 (Fig. 8c). The FLEXPART simulations over OHP show a denser volcanic plume, in terms
 606 of the SO₂ tracer, at altitudes of about 9-10 km altitude, with less dense volcanic plume at lower
 607 altitudes (2-4 km). This is generally consistent with the observations of the LTA LiDAR system
 608 at OHP (Figs. 8d-e). The LTA LiDAR was operational from about 18:30 to 22:30 on 24/04 and
 609 25/02; it observes an aerosol layer at about 10-11 km altitude on both days and during the full
 610 period, with a maximum value of the aerosol extinction between 19:00 and 21:00 on 24/02,
 611 consistently with FLEXPART simulations. The very weak volcanic aerosol signature at 10-11 km
 612 for LTA LiDAR observations 25/02 is not present in FLEXPART simulations. A previous
 613 observations session was carried out during the late afternoon/evening of 23/02 (not shown here);
 614 a volcanic-related aerosol plume is not observed during this period, consistently with FLEXPART

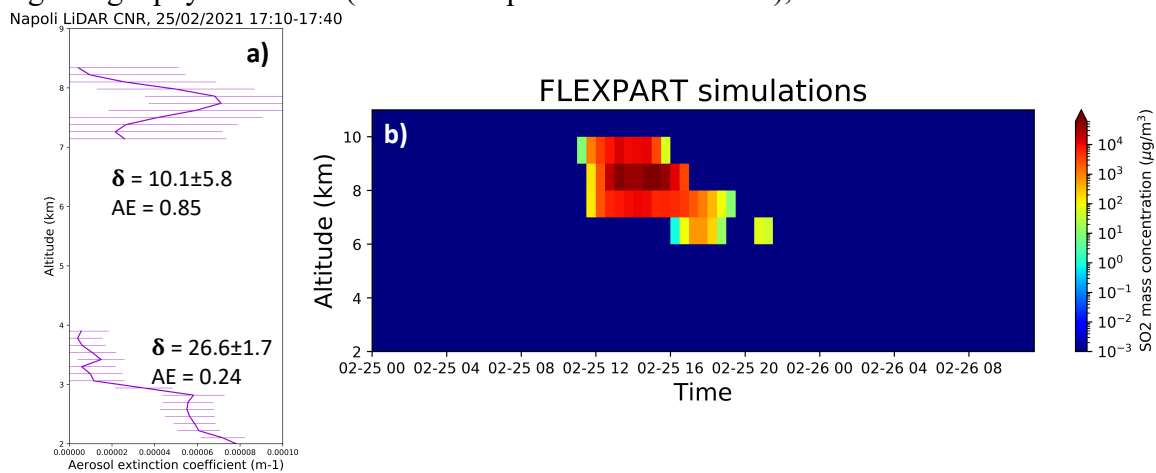
615 time-series analyses of the plume P2/W dispersion. While the LTA LiDAR system was operational
 616 only during night-time, the co-located GAIA system observed the atmosphere over OHP during
 617 day-time as well (data not shown here), even if with a significantly lesser signal/noise ratio at those
 618 altitudes. While GAIA observes the same night-time volcanic aerosol signature as LTA (discussed
 619 above), no aerosol signature is present during the days of 24 and 25/02, so it is reasonable to
 620 exclude that volcanic aerosols were present in the atmosphere over OHP during the day. Besides
 621 the relatively high-altitude aerosol layer observations, the LTA LiDAR observed a lower-altitude
 622 aerosol plume at 3-5 km (see Fig. 8a). This aerosol signal can be easily associated with the dust
 623 event described in Sect. 4.3, even if a component of volcanic aerosol cannot be excluded based on
 624 the FLEXPART vertical profiles of Fig. 8c. For a limited time, the LTA and the LiO3t LiDARs
 625 operated simultaneously at OHP. Using a combination of the aerosol backscattering profiles
 626 retrieved by LTA (at 532 nm) and the LiO3t (at 316 nm) LiDARs at OHP, a colour ratio has been
 627 calculated in the free troposphere on 24/02 between about 19:00 and 20:30. The aerosol
 628 backscattering profile observations at both wavelengths show a vertically thin plume at about 10-
 629 11 km and a wider plume between 3 and 5 km. Besides this quite distinct vertical structure, the
 630 colour ratio shows very different values for the two layers, with 0.1-0.2 for the highest first layer
 631 and up to 1.0-1.2 for the lowest layer. In addition, depolarisation ratio observations with the GAIA
 632 system for the highest layer display very small, near-zero values. These evidences indicate the
 633 presence of distinctly smaller mean particle size, with a possible spherical shape, for the highest
 634 layer with respect to the lowest, thus corroborating the possibility that volcanic aerosols, with an
 635 SA prevalence, and dust, respectively, dominate the two layers. Spectroscopic evidence of the
 636 presence of SA at OHP is found using the AEROIASI-H2SO4 retrieval algorithm (Supplementary
 637 Fig. 3), this suggesting that the volcanic plume P2/W is composed of SA, even if the presence of
 638 an ash fraction cannot be excluded.



639
 640 *Figure 8: Mean aerosol backscattering coefficient profiles, between 19:00 and 20:30 of the day 24/02/2021, observed by LiO3t*
 641 *(violet line) and LTA (green line) LiDARs (a), and the backscattering colour ratio (b), at OHP station. FLEXPART SO2 mass*
 642 *concentration profiles, from 24/02/2021 00:00 to 26/02/2021 12:00, over OHP station (c) and available night-time LTA*
 643 *observations of the aerosol extinction coefficient in the same period (d: 24/02; e: 25/02). Time intervals of LTA observations are*
 644 *indicated by black dashed lines in panel c.*

645 The P2/E plume section is observed at Napoli station. Based on the FLEXPART simulations, the
 646 P2/E volcanic plume overpasses Napoli during the period spanning from late morning to early

647 evening of 25/02, at an altitude of 7-10 km, with a maximum density between 15:00 to 18:00 (Fig.
 648 9b). Consistently, the LiDAR system in Napoli observed a vertically-confined aerosol plume in
 649 the afternoon of 25/02, with a maximum around 17:30, at 7-8 km (Fig. 9a). A second aerosol
 650 plume, with a wider vertical structure, is observed between 2 and 3 km. The LiDAR system in
 651 Napoli operates at two wavelengths and has depolarisation information (depolarization ratio δ).
 652 Using the two wavelengths, the bulk Ångström exponent (AE) has been calculated. Both AE and
 653 δ show distinct values for the two layers: AE of 0.85 and 0.24, and δ of $10.1 \pm 5.8\%$ and $26.6 \pm 1.7\%$,
 654 for the higher and lower layer, respectively. This indicates significantly smaller (AE observations)
 655 more spherical-shaped (δ) for the higher layer, thus corroborating the identification of the highest
 656 layer as volcanic and the lowest as dust. The AE and δ for the highest layer are nevertheless quite
 657 different from what expected for a pure SA-dominated layer, indicating the possibility of the
 658 presence of a fraction of larger and aspherical ash particles. It is also important to notice that: 1)
 659 the SO₂ plume tracer of P2/E in Napoli (Fig. 9b) has peak values nearly two orders of magnitude
 660 larger than for P2/W at OHP (Fig. 8c), and 2) the aerosol extinction is almost ten times larger for
 661 P2/E (Fig. 9a) than P2/W (Fig. 8d). This clearly indicates the large variability of the morphology
 662 and properties of one volcanic plume, e.g. when looking at different plume's sections.
 663 Based on the results shown in this section, two main evidences emerge: 1) precise (e.g. in terms
 664 of the input parameters) and detailed dispersion simulations, as well as complementary satellite
 665 observations at a wider regional scale, as support towards the interpretation of downwind
 666 observations, and 2) synoptic downwind observations at different locations, can be used to
 667 characterise in details confined plumes of known source and their variability in three-dimensional
 668 morphology, composition and properties. In the present case, for example, two separate and non-
 669 mixing vertical layers of volcanic aerosols and dust could be identified. For the volcanic aerosol
 670 layer, the variability of the vertical structure and composition at different sections of the plumes
 671 (see the case of plumes P2/W and P2/E), as well as the different properties of individual plumes
 672 for a given geophysical event (see the comparison of P1 and P2), could be characterised.



673
 674
 675
 676
 677
 Figure 9: Mean aerosol extinction coefficient profiles at 355 nm, between 17:10 and 17:40 of the day 25/02/2021, observed by LiDAR (a) and FLEXPART SO₂ mass concentration profiles, from 25/02/2021 00:00 to 26/02/2021 12:00, over Napoli station (b). The mean Ångström exponent (AE) and depolarisation ratio (δ), for the two identified vertically-separated aerosol layers are also reported in panel a.

678 4.5 Optical properties and the impact on the radiative balance

679 Using the observations from ground-based LiDAR and the complementary observations and
680 atmospheric modelling of the previous sections, the optical and radiative properties of plumes P1
681 and P2/E and W, at Sede Boker, OHP and Napoli stations, have been estimated.

682 The volcanic-specific aerosol optical depth (AOD_V), averaged during the core overpass periods
683 (see details in the caption of Tab. 1) at the three ground stations, estimated using LiDAR data, are
684 listed in Tab. 1. These values are also compared with the total column (i.e. volcanic plus dust and
685 other possible aerosols in the line of sight of the instrument) AOD_T , AE_T and SSA_T estimated with
686 co-located AERONET Cimel sun photometers. For plume P1, moderate AOD_T are found, with
687 relatively high AE_T , which points at a limited impact of dust in the overall column. The AOD_V is
688 relatively large, 0.0076 ± 0.0015 . As mentioned, the large δ_V , aggregated with a relatively large
689 AOD_V , may point at a consistent presence of ash within the identified volcanic plume P1. This is
690 somewhat surprising for a plume that, at the time of downwind observation, has already aged about
691 4-5 days since emissions. It is worth noticing that this plume shows a consistent descent during
692 the dispersion (emitted at about 12 km and detected at Sede Boker at 5 to 10 km) which can be
693 linked to the larger sedimentation rate of the more massive ash particles than SA. As already
694 discussed in the previous section, plume P2 looks very inhomogeneous, when comparing the
695 western and eastern ends P2/W and P2/E. This is mirrored by inhomogeneities in the measured
696 AOD_T . The P2/W plume has almost ten times smaller AOD_T with respect to P2/E (P2/W:
697 0.0036 ± 0.0014 , P2/E: 0.031 ± 0.006). As discussed in Sect. 4.4, this large difference in the AOD_T
698 of P2/W and E can be attributed to the fact that these plumes may be largely dominated by SA, the
699 first, and may present a fraction of ash, the second. With AOD_T between 0.25 and 0.30, the total
700 column looks largely dominated by dust, with the volcanic component taking only a small part of
701 the column. Relatively small AE_T seems to confirm this hypothesis through the indication of the
702 dominance of very large (dust) particles.

703 Using the libRadtran-UVSPEC radiative transfer model (RTM), driven by aerosol extinction
704 profiles measured by LiDARs at the three stations, the daily average radiative forcing (RF) of the
705 isolated volcanic plumes has been estimated with the methodology described in Sect. 2.2.2, and is
706 reported in Tab. 2. The aerosol extinction profiles used as input to the RTM are the average of the
707 observations at the core overpass time, i.e. the same period used to calculate the AOD_V in Tab.1
708 and detailed in its caption. Based on the considerations above and the complementary observations,
709 we have made the following hypotheses for non-measured optical parameters of the plumes. For
710 plume P1 at Sede Boker, a fraction of fine ash was probably present in the volcanic plume. Thus,
711 we have run the RTM using an interval of AE typical of small-sized particles (1.8-2.0) and a SSA
712 typical of partially absorbing particles (0.90-0.95). A moderately dusty background lower-
713 tropospheric atmosphere is considered for altitudes between surface to 3 km. For plume P2/W at
714 OHP, a SA-dominated plume is considered. Thus, we have run the RTM using an interval of AE
715 typical of small-sized particles (1.8-2.0) and a SSA typical of very reflective aerosols (0.95-1.00).
716 A very dusty background lower-tropospheric atmosphere is considered for altitudes between
717 surface to 5 km, based on LiDAR observations of the lowest layer of e.g. Fig. 8a-b. For plume
718 P2/E at Napoli, a fraction of ash in the volcanic plume is considered. Thus, we have run the RTM
719 using the observed AE (0.85), which is typical of larger particles than what found for P1 and P2/W,
720 and SSA typical of partly absorbing aerosols (0.90-0.95). As for plume P2/W, a very dusty
721 background lower-tropospheric atmosphere is considered for altitudes between surface to 5 km,
722 based on LiDAR observations of the lowest layer of e.g. Fig. 9a. With these assumptions, a TOA
723 RF of -0.22 ± 0.06 , -0.17 ± 0.03 and -1.19 ± 0.29 W/m², and a surface RF of -0.66 ± 0.09 , -0.21 ± 0.04

724 and -3.51 ± 0.47 W/m² are found for P1, P2/W and P2/E, respectively. Associated with a larger
 725 AOD_v, the RF of P2/E is significantly larger than for P1 and P2/W. The surface RF is much larger
 726 than the TOA RF, for both P1 and P2/E, due to the presence of absorbing aerosols in these plumes.
 727 This means that part of the incoming shortwave radiation does not reach the surface due to the in-
 728 plume absorption, which adds to the radiation scattered back to space. For plume P2/W, the TOA
 729 and surface RF have a very similar value, which points at a very limited absorption within the
 730 plume due to the likely dominant presence of purely reflective SA. The RF values obtained for
 731 these plumes can be compared with RFs estimated in the past for proximal and distal observations
 732 of Mount Etna's emissions. Using ground LiDAR observations as input to the RTM, Sellitto et al.
 733 (2020) have estimated the RF of a typical passive degassing plume at a proximal location, about 7
 734 km downwind Mount Etna craters and have found values of about -4.5 and -7.0 W/m², at TOA
 735 and surface. Mild explosions and a small fraction of ash were present during these observations.
 736 For an almost purely SA, after a dispersion of about 350 km downwind Mount Etna, Sellitto et al.
 737 (2016) have found a RF efficiency, i.e. the RF per AOD unit, of about -40 to -50 W/m²/AOD. The
 738 RF efficiency of P2/E (about 35 W/m²/AOD) and P1 (about 29 W/m²/AOD) are consistent with
 739 estimations of Sellitto et al. (2020) for an ashy passive degassing plume (about 35 W/m²/AOD).
 740 The RF efficiency of P2/W (about 47 W/m²/AOD) is consistent with estimations of Sellitto et al.
 741 (2016) for purely SA plume. Compared with larger volcanic eruptions, our estimates are e.g. of
 742 the same order of magnitude or even larger than the impact of the Raikoke eruption in 2019 (-0.3
 743 to -0.4 W/m²) (Kloss et al., 2021). The Raikoke had the largest volcanic impact on the radiative
 744 balance documented in at least the last 3 years. Of course, Raikoke eruption is much more relevant
 745 than the activity of Mount Etna discussed in the present study, due to its larger scale (hemispheric)
 746 impact. This demonstrates that, even if Mount Etna eruptions are of a limited regional interest,
 747 they can have a quite relevant impact at the regional scale.

748
 749 *Table 1: Summary of optical properties of volcanic plumes P1 and P2, volcanic-specific layers (V index in the table) from LiDAR*
 750 *observations and total-column values (T index in the table) from AERONET sun-photometric observations. *=mean value of*
 751 *LiDAR observations between 25/02 20:00 and 26/02 06:00; **=mean value of sun-photometric observations of 25 and 26/02;*
 752 ****=mean value of sun-photometric observations of 26/02 between 05:00 and 06:00; §=mean value of LTA LiDAR observations*

753 of 24/02 between about 19:00 and 21:30; ^{§§}=mean value of sun-photometric observations of 24/02; += mean value of LiDAR
 754 observations of 25/02 between 17:10 and 17:40 (as in Fig. 9); ⁺⁺=mean value of sun-photometric observations of 25/02

	AOD _V (532 nm)	δ _V (532 nm)	AE _V	AOD _T (532 nm)	AE _T	SSA _T
P1: Sede Boker	0.0076±0.0015* (maximum: 0.035)	32.3±1.4%*	-	0.099±0.004** 0.116±0.005***	1.16±0.01***	0.88±0.01***
P2/W: OHP observatory	0.0036±0.0014 [§] (maximum: 0.0062)	-	-	0.26±0.06 ^{§§}	0.21±0.10 ^{§§}	0.96±0.03 ^{§§}
P2/E: Napoli Observatory	0.031±0.006 ⁺	10.1±5.8% ⁺	0.85 ± 0.60 ⁺	0.310±0.070 ⁺⁺	0.92±0.12 ⁺⁺	0.94±0.02 ⁺⁺

755

756 Table 2: Summary of radiative forcing estimations of volcanic plumes P1 and P2, see text for the radiative transfer modelling
 757 setup and hypotheses

	TOA radiative forcing (W/m ²)	Surface radiative forcing (W/m ²)
P1: Sede Boker	-0.22±0.06	-0.66±0.09
P2/W: OHP observatory	-0.17±0.03	-0.21±0.04
P2/E: Napoli Observatory	-1.19±0.29	-3.51±0.47

758

759 5 Conclusions

760 The synergy of volcanic plumes observation and modelling at different spatio-temporal scales is
 761 crucial to characterize their emission, dispersion and downwind impacts. Mount Etna experiences
 762 an intense eruptive activity between February and April 2021. Within this phase, three peculiar
 763 extreme events, in terms of the large SO₂ emission rates (55 kt of SO₂ emitted overall) and
 764 injection altitude (up to 12 km), took place between 21 and 26/02, that we have studied with a
 765 combination of regional-scale satellite observations and Lagrangian dispersion modelling, and
 766 local downwind measurement at selected ground stations coupled with offline RTM modelling.
 767 These three events and the subsequently formed plumes of volcanic effluents (plumes P1-3)
 768 displayed a very uncommon dispersion towards the north, which allowed the downwind
 769 observation and characterisation of the plumes due to the presence of several observatory sites in
 770 this quadrant. Ground-based LiDAR observations and complementary information from
 771 observations and modelling at the sites of Sede Boker, Israel (plume P1), OHP (western end of
 772 plume P2 – P2/W) and Napoli (eastern end of plume P2 – P2/E) revealed a complex inter- (P1
 773 versus P2) and intra-plume (P2/W versus P2/E) variability of the morphology, composition, optical
 774 properties and radiative impacts of Mount Etna plumes. Plume P1 has been detected at about 10
 775 then descending to 5-6 km after only 4-5 days atmospheric aging, with depolarisation ratio
 776 consistent with a possible presence of in-plume ash. Plume P2 displayed a dramatic variability
 777 from east to west ends, with a thin and likely SA-dominated plume to the west and a dense and
 778 likely ash-bearing plume to the east. Both the AOD (0.004 to 0.03) and local clear-sky daily

779 average shortwave radiative forcing (-0.2 to -1.2 W/m^2 , at TOA and -0.2 to -3.5 W/m^2 at the
 780 surface) point at a very relevant impact on the upper-tropospheric aerosol layer and the regional
 781 climate at the continental scale, in the Mediterranean. In addition, the synergy of observations and
 782 modelling presented in the present work allowed to empirically disentangle the information about
 783 volcanic aerosols and other aerosol sources, like mineral dust.

784 **Acknowledgments, Samples, and Data**

785 This work has been funded by: CNES (Centre National d'Études Spatiales) via TOSCA/IASI
 786 grant; CNRS (Centre national de la recherche scientifique)-INSU(Institut National des Sciences
 787 de l'Univers) PNTS (Programme National de Télédétection Spatiale) via MIA-SO2 grant. This
 788 work benefited from the support of the ACTRIS-Fr Infrastructure and ENSG (Ecole Nationale des
 789 Sciences Géographiques) at the OHP site. Stefano Corradini, Luca Merucci, Daniele Stelitano and
 790 Lorenzo Guerrieri work was supported by the ESA project VISTA (Volcanic monitoring using
 791 SenTinel sensors by an integrated Approach), grant number 4000128399/19/I-DT and by the
 792 INGV project IMPACT. IASI is a joint mission of EUMETSAT and the Centre National d'Études
 793 Spatiales (CNES, France). The authors acknowledge the AERIS data infrastructure for providing
 794 access to the IASI SO2, and IASI Level 1c and AVHRR-CLARA2 data, inputs to the AEROIASI
 795 algorithms. The authors acknowledge ULB-LATMOS for the development of the IASI SO2
 796 retrieval algorithm. The ECMWF is acknowledged for providing the meteorological analyses used
 797 for both AEROIASI observations and the FLEXPART simulations. The authors thank Pierre-Eric
 798 Blanc and Baptiste Camus for their technical support on the OHP GAIA system. They are grateful
 799 to Philippe Goloub and Ioana Popovici at Laboratoire Optique de Lille for their advices regarding
 800 the treatment of the GAIA datasets. The PIs of the PHOTON-AERONET stations of OHP
 801 (Philippe Goloub and Thierry Podvin), Napoli (Nicola Spinelli) and Sede Boker (Arnold Karnieli)
 802 are gratefully acknowledged.

803 **References**

- 804 Ancellet G. and Beekmann M. (1997) Evidence for changes in the ozone concentrations in the
 805 free troposphere over southern France from 1976 to 1995, *Atmospheric Environment*, 31, 17,
 806 2835-2851, [https://doi.org/10.1016/S1352-2310\(97\)00032-0](https://doi.org/10.1016/S1352-2310(97)00032-0).
- 807 Andersson, S., Martinsson, B., Vernier, JP. et al. (2015) Significant radiative impact of volcanic
 808 aerosol in the lowermost stratosphere. *Nat. Commun.* 6, 7692.
 809 doi:<https://doi.org/10.1038/ncomms8692>
- 810 Ansmann, A., Riebesell, M., and Weitkamp, C. (1990) Measurement of atmospheric aerosol
 811 extinction profiles with a Raman lidar. *Opt. Lett.*, 15, 746–748. doi:10.1364/OL.15.000746.
- 812 Biele, J., Beyerle, G., and Baumgarten, G. (2000) Polarization lidar: corrections of instrumental
 813 effects. *Opt. Express*, 7, 427–435, doi:10.1364/OE.7.000427.
- 814 Biermann, U.M., Luo, B.P., Peter, T. (2000) Absorption Spectra and Optical Constants of Binary
 815 and Ternary Solutions of H₂SO₄, HNO₃, and H₂O in the Mid Infrared at Atmospheric
 816 Temperatures. *J. Phys. Chem. A*, 104, 783–793.
- 817 Bilal, M.; Nazeer, M.; Nichol, J.; Qiu, Z.; Wang, L.; Bleiweiss, M.P.; Shen, X.; Campbell, J.R.;
 818 Lolli, S. Evaluation of Terra-MODIS C6 and C6.1 Aerosol Products against Beijing, XiangHe,
 819 and Xinglong AERONET Sites in China during 2004-2014. *Remote Sens.* 2019, 11, 486.
 820 <https://doi.org/10.3390/rs11050486>.

- 821 Boselli, A., D'Emilio, M., Sannino, A., Wang, X., and Amoruso, S. (2021) Remote sensing and
822 near surface observations of aerosol properties measured in real time during a big fire event on
823 Mount Vesuvius, *Remote Sensing*, 13(10), <https://doi.org/10.3390/rs13102001>.
- 824 Campbell, J.R. J.R., D.L. Hlavka, E.J. Welton, C.J. Flynn, D.D. Turner, J.D. Spinhirne, V.S.
825 Scott, and I.H. Hwang, 2002. Full-time, Eye-Safe Cloud and Aerosol Lidar Observation at
826 Atmospheric Radiation Measurement Program Sites: Instrument and Data Processing, *J. Atmos.*
827 *Oceanic Technol.*, 19, 431-442.
- 828 Campbell, J. R., Dolinar, E. K., Lolli, S., Fochesatto, G. J., Gu, Y., Lewis, J. R., ... & Welton, E.
829 J. (2021). Cirrus cloud top-of-the-atmosphere net daytime forcing in the Alaskan subarctic from
830 ground-based MPLNET monitoring. *Journal of Applied Meteorology and Climatology*, 60(1),
831 51-63.
- 832 Clarisse, L., Hurtmans, D., Clerbaux, C., Hadji-Lazaro, J., Ngadi, Y., and Coheur, P.-F. (2012)
833 Retrieval of sulphur dioxide from the infrared atmospheric sounding interferometer (IASI),
834 *Atmos. Meas. Tech.*, 5, 581–594, <https://doi.org/10.5194/amt-5-581-2012>.
- 835 Clarisse, L., Coheur, P.-F., Theys, N., Hurtmans, D., and Clerbaux, C. (2014) The 2011 Nabro
836 eruption, a SO₂ plume height analysis using IASI measurements, *Atmos. Chem. Phys.*, 14,
837 3095–3111, <https://doi.org/10.5194/acp-14-3095-2014>.
- 838 Clerbaux, C., Boynard, A., Clarisse, L., George, M., Hadji-Lazaro, J., Herbin, H., Hurtmans, D.,
839 Pommier, M., Razavi, A., Turquety, S., et al. (2009) Monitoring of atmospheric composition
840 using the thermal infrared IASI/MetOp sounder. *Atmos. Chem. Phys.*, 9, 6041–6054.
- 841 Corradini S.; Guerrieri L.; Lombardo V.; Merucci L.; Musacchio M., Prestifilippo M.; Scollo S.;
842 Silvestri M.; Spata G.; Stelitano D. (2018) Proximal monitoring of the 2011-2015 Etna lava
843 fountains using MSG-SEVIRI data. *MDPI Geosciences*, 8, 140;
844 [doi:10.3390/geosciences8040140](https://doi.org/10.3390/geosciences8040140)
- 845 Corradini S., Guerrieri L., Stelitano D., Salerno G., Scollo S., Merucci L., Prestifilippo M.,
846 Musacchio M., Silvestri M., Lombardo V., Caltabiano T. (2020) Near Real-Time Monitoring of
847 the Christmas 2018 Etna Eruption Using SEVIRI and Products Validation, *Remote Sens.*, 12,
848 1336; [doi:10.3390/rs12081336](https://doi.org/10.3390/rs12081336).
- 849 Corradini S., Guerrieri L., Brenot H., Clarisse L., Merucci L., Pardini F., Prata A.J., Realmuto
850 V.J., Stelitano D., Theys N. (2021) Tropospheric Volcanic SO₂ Mass and Flux Retrievals from
851 Satellite. The Etna December 2018 Eruption”, *Remote Sens.*, 13, 2225.
852 <https://doi.org/10.3390/rs13112225>.
- 853 Cuesta, J., Eremenko, M., Flamant, C., Dufour, G., Laurent, B., Bergametti, G., Höpfner, M.,
854 Orphal, J., Zhou, D. (2015) Three-dimensional distribution of a major desert dust outbreak over
855 East Asia in March 2008 derived from IASI satellite observations. *J. Geophys. Res. Atmos.*, 120,
856 7099–7127.
- 857 Cuesta, J., Flamant, C., Gaetani, M., et al. (2020) Three-dimensional pathways of dust over the
858 Sahara during summer 2011 as revealed by new Infrared Atmospheric Sounding Interferometer
859 observations. *Q J R Meteorol Soc.*; 146: 2731– 2755. <https://doi.org/10.1002/qj.3814>
- 860 Di Biagio, C., Formenti, P., Balkanski, Y., Caponi, L., Cazaunau, M., Panguì, E., Journet, E.,
861 Nowak, S., Caquineau, S., Andreae, M. O., Kandler, K., Saeed, T., Piketh, S., Seibert, D.,
862 Williams, E., and Doussin, J.-F. (2017) Global scale variability of the mineral dust long-wave

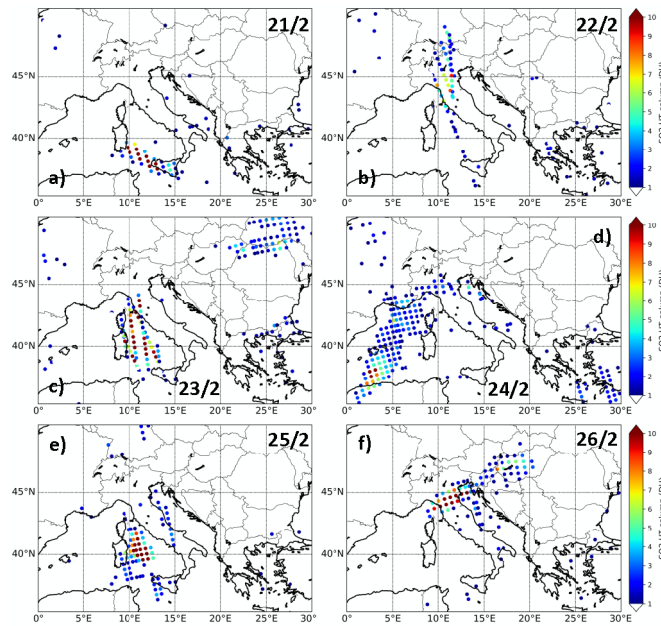
- 863 refractive index: a new dataset of in situ measurements for climate modeling and remote sensing,
864 *Atmos. Chem. Phys.*, 17, 1901–1929, <https://doi.org/10.5194/acp-17-1901-2017>.
- 865 M. Dittman et al. (2002), Nadir ultraviolet imaging spectrometer for the NPOESS Ozone
866 Mapping and Profiler Suite (OMPS), *Proc. SPIE*, 4814.
- 867 Emde, C., Buras-Schnell, R., Kylling, A., Mayer, B., Gasteiger, J., Hamann, U., Kylling, J.,
868 Richter, B., Pause, C., Dowling, T., and Bugliaro, L. (2016) The libRadtran software package for
869 radiative transfer calculations (version 2.0.1), *Geosci. Model Dev.*, 9, 1647–1672,
870 <https://doi.org/10.5194/gmd-9-1647-2016>.
- 871 Fernald, F. G. "Analysis of atmospheric lidar observations: some comments." *Applied optics*
872 23.5, 1984: 652-653.
- 873 Freudenthaler, V., Esselborn, M., Wiegner, M., Heese, B., Tesche, M., and Ansmann, A. (2009)
874 Depolarization ratio profiling at several wavelengths in pure Saharan dust during SAMUM 2006.
875 *Tellus* 2009, 61B, 165–179. Doi: 10.1111/j.16000889.2008.00396.x.
- 876 Gaudel A., Ancellet G., Godin-Beekmann S. (2015) Analysis of 20 years of tropospheric ozone
877 vertical profiles by lidar and ECC at Observatoire de Haute Provence (OHP) at 44°N, 6.7°E,
878 *Atmospheric Environment*, 113, 78-89, <https://doi.org/10.1016/j.atmosenv.2015.04.028>.
- 879 Guerrazi, H., Sellitto, P., Cuesta, J., Eremenko, M., Lachatre, M., Mailler, S., Carboni, E.,
880 Salerno, G., Caltabiano, T., Menut, L., Serbaji, M.M., Rekhiss, F., Legras, B. (2021)
881 Quantitative Retrieval of Volcanic Sulphate Aerosols from IASI Observations. *Remote Sens.*,
882 13, 1808. <https://doi.org/10.3390/rs13091808>
- 883 Guerrieri, L., Merucci, L., Corradini, S., Pugnaghi, S. (2015) Evolution of the 2011 Mt. Etna ash
884 and SO₂ lava fountain episodes using SEVIRI data and VPR retrieval approach. *J. Volcanol.*
885 *Geotherm. Res.*, 291, 63–71.
- 886 Haywood, J. M., Jones, A., Clarisse, L., Bourassa, A., Barnes, J., Telford, P. et al. (2010),
887 Observations of the eruption of the Sarychev volcano and simulations using the HadGEM2
888 climate model, *Journal of Geophysical Research*, 115, D21212, doi:10.1029/2010JD014447.
- 889 Holben, B.; Eck, T.; Slutsker, I.; Tanré, D.; Buis, J.; Setzer, A.; Vermote, E.; Reagan, J.;
890 Kaufman, Y.; Nakajima, T.; et al. (1998) AERONET—A Federated Instrument Network and
891 Data Archive for Aerosol Characterization. *Remote Sens. Environ.*, 66, 1–16.
- 892 Hoshyariapour, A. (2021) February 2021: A dusty month for Europe
893 <https://blogs.egu.eu/divisions/as/2021/04/03/february-2021-a-dusty-month-for-europe/>
- 894 Khaykin, S. M et al. (2017) Variability and evolution of the midlatitude stratospheric aerosol
895 budget from 22 years of ground-based lidar and satellite observations, *Atmos. Chem. Phys.*, 17,
896 1829–1845, <https://doi.org/10.5194/acp-17-1829-2017>.
- 897 Kearney, C.S.; Watson, I.M. (2009) Correcting satellite-based infrared sulfur dioxide retrievals
898 for the presence of silicate ash., *J. Geophys. Res. Space Phys.*, 114, 22208.
- 899 Keckhut P., Hauchecorne A., and Chanin, M.L. (1993) A critical review on the data base
900 acquired for the long term surveillance of the middle atmosphere by French Rayleigh lidars, *J.*
901 *Atmos. Oceanic Technol.*, 10, 850-867.

- 902 Lewis, J.R., J.R. Campbell, E.J. Welton, S.A. Stewart, and P.C. Haftings (2016). Overview of
903 MPLNET Version 3 Cloud Detection. *J. Atmos. Oceanic Tech.*, 33, 2113 – 2134, doi:
904 10.1175/JTECH-D-15-0190.1.
- 905 Lolli, S.; D’Adderio, L.; Campbell, J.; Sicard, M.; Welton, E.; Binci, A.; Rea, A.; Tokay, A.;
906 Comerón, A.; Baldasano, R.B.J.M.; et al. Vertically Resolved Precipitation Intensity Retrieved
907 through a Synergy between the Ground-Based NASA MPLNET Lidar Network Measurements,
908 Surface Disdrometer Datasets and an Analytical Model Solution. *Remote Sens.* 2018, 10, 1102
- 909 Lolli, S.; Vivone, G.; Lewis, J.R.; Sicard, M.; Welton, E.J.; Campbell, J.R.; Comerón, A.;
910 D’Adderio, L.P.; Tokay, A.; Giunta, A.; Pappalardo, G. Overview of the New Version 3 NASA
911 Micro-Pulse Lidar Network (MPLNET) Automatic Precipitation Detection Algorithm. *Remote*
912 *Sens.* 2020, 12, 71. <https://doi.org/10.3390/rs12010071>
- 913 Klett JD. Stable analytical inversion solution for processing lidar returns. *Appl Opt.* 1981 Jan
914 15;20(2):211-20. doi: 10.1364/AO.20.000211. PMID: 20309093.
- 915 Kloss, C., Berthet, G., Sellitto, P., Ploeger, F., Taha, G., Tidiga, M. et al. (2021). Stratospheric
916 aerosol layer perturbation caused by the 2019 Raikoke and Ulawun eruptions and their radiative
917 forcing, *Atmospheric Chemistry and Physics*, 21, 535–560, [https://doi.org/10.5194/acp-21-535-](https://doi.org/10.5194/acp-21-535-2021)
918 2021.
- 919 Krotkov, N. A., Krueger, A. J. & Bhartia, P. K. (1997). Ultraviolet optical model of volcanic
920 clouds for remote sensing of ash and sulfur dioxide. *Journal of Geophysical Research:*
921 *Atmospheres*, 102, 21891–21904. <https://doi.org/10.1029/97JD01690>.
- 922 Malavelle, F. F., Haywood, J. M., Jones, A., Gettelman, A., Clarisse, L., Bauduin, S. et al. (2017)
923 Strong constraints on aerosol–cloud interactions from volcanic eruptions. *Nature*, 546, 485–491.
- 924 Merucci, L.; Burton, M.; Corradini, S.; Salerno, G. (2011) Reconstruction of SO₂ flux emission
925 chronology from space-based measurements. *J. Volcanol. Geotherm. Res.*, 206, 80–87.
926 doi:10.1016/j.jvolgeores.2011.07.002.
- 927 Michaud, J., Krupitsky, D., Grove, J. & Anderson, B. (2005). Volcano related atmospheric
928 toxicants in Hilo and Hawaii Volcanoes National Park: Implications for human health.
929 *Neurotoxicology*, 26, 555–563. <https://doi.org/10.1016/j.neuro.2004.12.004>.
- 930 Oppenheimer, C., Scaillet, B., & Martin, R. S. (2011). Sulfur Degassing From Volcanoes:
931 Source Conditions, Surveillance, Plume Chemistry and Earth System Impacts, *Reviews in*
932 *Mineralogy and Geochemistry*, 72, 363–421, doi:10.2138/rmg.2011.73.13, 2011.
- 933 Pisso, I. et al. (2019) The Lagrangian particle dispersion model FLEXPART version 10.4,
934 *Geosci. Model Dev.*, 12, 4955–4997, <https://doi.org/10.5194/gmd-12-4955-2019>.
- 935 Prata, A. T., Young, S. A., Siems, S. T., & Manton, M. J. (2017). Lidar ratios of stratospheric
936 volcanic ash and sulfate aerosols retrieved from CALIOP measurements. *Atmospheric*
937 *Chemistry and Physics*, 17(13), 8599-8618.
- 938 Ridley, D. A., Solomon S., Barnes, J. E., Burlakov, V. D., Deshler, T., Dolgii, S. I. et al. (2014),
939 Total volcanic stratospheric aerosol optical depths and implications for global climate change,
940 *Geophysical Research Letters*, 41, 7763– 7769, doi:10.1002/2014GL061541.

- 941 Santer, B. D., Bonfils, C., Painter, J. F., Zelinka, M. D., Mears, C., Solomon, S. et al. (2014).
942 Volcanic contribution to decadal changes in tropospheric temperature. *Nature Geoscience*, 7,
943 185–189.
- 944 Scollo, S.; Prestifilippo, M.; Spata, G.; D’Agostino, M., Coltelli, M. (2009) Monitoring and
945 forecasting Etna volcanic plumes. *Nat. Hazards Earth Syst. Sci.*, 9, 1573–1585.
- 946 Sellitto, P. & Briole, P. (2015). On the radiative forcing of volcanic plumes: Modelling the
947 impact of Mount Etna in the Mediterranean. *Annals of Geophysics*, 58.
948 <https://doi.org/10.4401/ag-6879> (2015).
- 949 Sellitto, P., di Sarra, A., Corradini, S., Boichu, M., Herbin, H., Dubuisson, P., et al. (2016).
950 Synergistic use of Lagrangian dispersion and radiative transfer modelling with satellite and
951 surface remote sensing measurements for the investigation of volcanic plumes: the Mount Etna
952 eruption of 25–27 October 2013, *Atmospheric Chemistry and Physics*, 16, 6841–6861,
953 <https://doi.org/10.5194/acp-16-6841-2016>.
- 954 Sellitto, P., Zanetel, C., di Sarra, A., Salerno, G., Tapparo, A. et al. (2017a) The impact of Mount
955 Etna sulfur emissions on the atmospheric composition and aerosol properties in the central
956 Mediterranean: A statistical analysis over the period 2000–2013 based on observations and
957 Lagrangian modelling. *Atmospheric Environment*, 148, 77–88.
958 <https://doi.org/10.1016/j.atmosenv.2016.10.032>.
- 959 Sellitto, P., Salerno, G., La Spina, A., Caltabiano, T., Scollo, S., Boselli, A. et al. (2020). Small-
960 scale volcanic aerosols variability, processes and direct radiative impact at Mount Etna during
961 the EPL-RADIO campaigns. *Scientific Reports*, 10, 15224. <https://doi.org/10.1038/s41598-020-71635-1>
- 962
- 963 Stelitano D., Corradini S., Merucci L., Guerrieri L. (2020) Procedure automatiche per la
964 rilevazione e la stima dei parametri delle nubi vulcaniche da satellite, MISCELLANEA INGV,
965 Progetto “Sale Operative Integrate e Reti di monitoraggio del futuro: l’INGV 2.0”. Report finale,
966 ISSN 1590-2595, 57. <https://doi.org/10.13127/misc/57/20>
- 967
- 967 Stevenson, D. S., Johnson, C. E., Collins, W. J. & Derwent, R. G. (2003). The tropospheric
968 sulphur cycle and the role of volcanic SO₂. *Geological Society of London Special Publication*,
969 213, 295–305. <https://doi.org/10.1144/GSL.SP.2003.213.01.18>.
- 970
- 970 Stiller, G. The Karlsruhe Optimized and Precise Radiative Transfer Algorithm (KOPRA) (2000)
971 Wissenschaftliche Berichte, FZKA; Forschungszentrum Karlsruhe: Karlsruhe, Germany, 2000.
- 972
- 972 Theys, N., I. De Smedt, H. Yu, T. Danckaert, J. van Gent, C. Hörmann, T. Wagner, P. Hedelt, H.
973 Bauer, F. Romahn, M. Pedergnana, D. Loyola, M. Van Roozendael (2017) Sulfur dioxide
974 operational retrievals from TROPOMI onboard Sentinel-5 Precursor: Algorithm Theoretical
975 Basis, *Atmos. Meas. Tech.*, 10, 119–153, doi:10.5194/amt-10-119-2017.
- 976
- 976 Veefkind, J.P., Aben, I., McMullan, K., Förster, H., De Vries, J., Otter, G., Claas, J.,
977 Eskes, H.J., De Haan, J.F., Kleipool, Q., Van Weele, M., Hasekamp, O., Hoogeveen, R.,
978 Landgraf, J., Snel, R., Tol, P., Ingmann, P., Voors, R., Kruizinga, B., Vink, R., Visser, H., and
979 Levelt, P.F. (2012). TROPOMI on the ESA Sentinel-5 Precursor: A GMES mission for
980 global observations of the atmospheric composition for climate, air quality and ozone
981 layer applications. *Remote Sensing of Environment*, 120: 70–83.
982 doi:10.1016/j.rse.2011.09.027

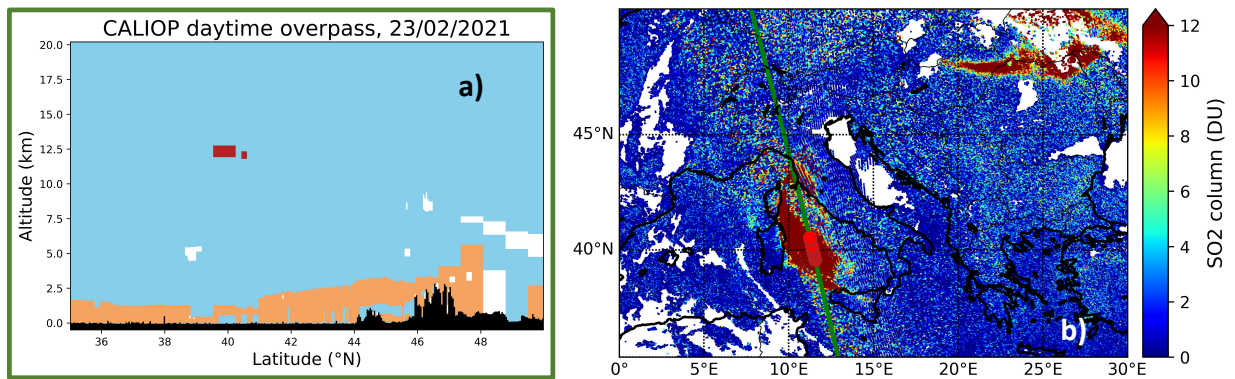
- 983 von Glasow, R., Bobrowski, N. & Kern, C. (2009), The effects of volcanic eruptions on the
984 atmospheric chemistry. *Chemical Geology*, 263, 131–142.
985 <https://doi.org/10.1016/j.chemgeo.2008.08.020>.
- 986 Wandinger, U., Nicolae, D., Pappalardo, G., Mona, L., Comerón, A. (2020) ACTRIS and its
987 aerosol remote sensing component, EPJ Web Conferences 237, 05003,
988 <https://doi.org/10.1051/epjconf/202023705003>.
- 989 Webley, P. W., Steensen, T., Stuefer, M., Grell, G., Freitas, S., & Pavolonis, M. (2012).
990 Analyzing the Eyjafjallajökull 2010 eruption using satellite remote sensing, lidar and WRF-
991 Chem dispersion and tracking model, *Journal of Geophysical Research: Atmospheres*, 117,
992 D00U26, doi:10.1029/2011JD016817.
- 993 Welton, E.J. K.J. Voss, H.R. Gordon, H. Maring, A. Smirnov, B. Holben, B. Schmid, J.M.
994 Livingston, P.B. Russell, P.A. Durkee, P. Formenti, M.O. Andreae (2000). Ground-based Lidar
995 Measurements of Aerosols During ACE-2: Instrument Description, Results, and Comparisons
996 with other Ground-based and Airborne Measurements, *Tellus B*, 52, 635-650.
- 997 Welton, E.J.; Campbell, J.R.; Spinhirne, J.D.; Stanley Scott, V., III. (2001). Global monitoring of
998 clouds and aerosols using a network of micropulse lidar systems. *SPIE Conf. Proc.*, 4153, 151–
999 158
- 1000 Welton, E.J., S.A. Stewart, J.R. Lewis, L.R. Belcher, J.R. Campbell, and S. Lolli (2018). Status
1001 of the NASA Micro Pulse Lidar Network (MPLNET): Overview of the network and future plans,
1002 new Version 3 data products, and the polarized MPL. EPJ Web of Conferences, 176,
1003 <https://doi.org/10.1051/epjconf/201817609003>.
- 1004 Wielicki, B.A., Cess, R.D., King, M.D., Randall, D.A., Harrison, E.F (1995) Mission to planet
1005 Earth: Role of clouds and radiation in climate. *Bull. Am. Meteorol. Soc.*, 76, 2125–2154
- 1006 Winker, D.M., Pelon, J., Coakley, J.A., Ackerman, S.A., Charlson, R.J., Colarco, P.R., Flamant,
1007 P., Fu, Q., Hoff, R.M., Kittaka, C. et al. (2010) The CALIPSO Mission. *Bull. Am. Meteorol.*
1008 *Soc.* 91, 1211–1230.

1009 **Supplementary Information**



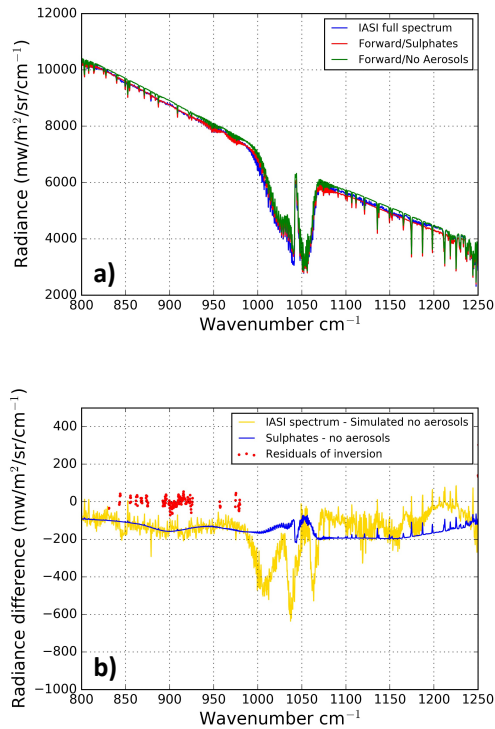
Supplementary Figure 1: OMPS-NM upper-tropospheric SO₂ observations from 21 (panel a) to 26/02/2021 (panel f).

1010
1011



Supplementary Figure 2: (a) Feature layer classification (same color code as in Fig. 6) for CALIOP daytime overpass, at ~1:30 pm, for 23/02/2021. (b) Sentinel-5p TROPOMI SO₂ column observations for 23/02/2021. The green line in panel b is the ground track of CALIOP observations of panel a. The position of the stratospheric aerosol (volcanic) feature, identified in panel a, is also indicated in panel b as red circles.

1012
1013
1014
1015
1016



1017
 1018
 1019
 1020
 1021
 1022
 1023
 1024

Supplementary Figure 3: The IASI spectrum (blue) taken at OHP (longitude: 5.74°E , latitude: 43.93°N) observed during daytime IASI overpass on 24/02/2021, the AEROIASI- H_2SO_4 fitted spectrum (red) and a fitted spectrum without SA (green). Spectral radiance differences of the IASI observed spectrum and the fitted spectrum without SA (yellow), the fitted spectra with and without SA (blue) and the fitting residuals (red dots). The SA size distribution is a log-normal with $0.5 \mu\text{m}$ mean size and 0.5 standard deviation. A mixing ratio of the sulphuric acid of 57% has been considered. The observed spectral signature of SA is observed in the range $800\text{-}950 \text{ cm}^{-1}$. For more details please refer to Guerrazi et al. (2021). The thermal infrared SA-specific AOD retrieval for this observation is 0.05.